AMBIENT SEISMIC NOISE INTERFEROMETRY ON THE ISLAND OF HAWAI‘I

A DISSERTATION SUBMITTED TO THE GRADUATE DIVISION OF THE UNIVERSITY OF HAWAI‘I AT MĀNOA IN PARTIAL FULFILLMENT OF THE REQUIREMENTS FOR THE DEGREE OF

DOCTOR OF PHILOSOPHY

IN

GEOLOGY AND GEOPHYSICS

MAY 2017

By

Silke Ballmer

Dissertation Committee:

Cecily J Wolfe, Chairperson
Robert A Dunn, Chairperson
Paul G Okubo
Fred K Duennebier
John M Sinton
Ian N Robertson

Keywords: Ambient seismic noise interferometry, Hawaii, Kilauea, volcanic tremor, volcano monitoring, surface wave tomography

ACKNOWLEDGMENTS

This thesis has not only spanned a certain amount of time, it has also moved with me to different locations, first from Honolulu to Tokyo, Japan and then to Zurich, Switzerland. Especially with regard to the difficulty of mentoring remotely, I would like to express my gratitude to my two advisors Cecily Wolfe and Robert Dunn for their invaluable support and guidance throughout this process, both scientifically as well as on a personal level. They were great mentors and colleagues and always had my best interest in mind. I am also thankful to all members of my doctoral committee for their never-ending patience and encouragement, particularly during the leave of absence while I was living in Japan, and during the following final stretch of the project.

Further, I am thankful to the Hawaiian Volcano Observatory (HVO) in general, and Paul Okubo in particular for providing me with access to the seismic dataset used for this work. I am also indebted to Matt Haney for sharing his expertise on the method, and codes for data analysis that tremendously helped me getting started with the project. The technical support of the School of Ocean and Earth Science and Technology, the RCF, especially Pat Townsend also deserves many thanks: first, for having spent endless hours on troubleshooting problems with the data storage unit, and later, for helping with data transfer so that I was able to take the huge amount of data with me when I moved abroad.

A big thanks goes to Geowatt AG, Zurich for offering me an office space and great company during the final stage of the project – the professional environment I needed to complete this dissertation. Thanks to David Trang, I had a home while visiting Hawai‘i in Fall 2016. I would also like to mention those special people that provided so much more than moral support and their friendship: Svetlana Natarov, Jean Verrette, Jeff Delmerico, Arjun Aryal and Erin Fitch. Finally, my husband Maxim was by my side every day of this process - I would not have made it without him. Thank you.

Financially, this work was supported by the National Science Foundation (NSF grant EAR-0910469 awarded to Cecily Wolfe), a fellowship from the U.S. Geological Survey awarded through the Hawaiian Volcano Observatory, and a fellowship from the German Academic Exchange Service (DAAD-*Doktorandenstipendium* D/11/42140).

ABSTRACT

Ambient seismic noise interferometry has been successfully applied in a variety of tectonic settings to gain information about the subsurface. As a passive seismic technique, it extracts the coherent part of ambient seismic noise in-between pairs of seismic receivers. Measurements of subtle temporal changes in seismic velocities, and high-resolution tomographic imaging are then possible – two applications of particular interest for volcano monitoring. Promising results from other volcanic settings motivate its application in Hawai‘i, with this work being the first to explore its potential. The dataset used for this purpose was recorded by the Hawaiian Volcano Observatory’s permanent seismic network on the Island of Hawai‘i. It spans 2.5 years from 5/2007 to 12/2009 and covers two distinct sources of volcanic tremor. After applying standard processing for ambient seismic noise interferometry, we find that volcanic tremor strongly affects the extracted noise information not only close to the tremor source, but unexpectedly, throughout the island-wide network. Besides demonstrating how this long-range observability of volcanic tremor can be used to monitor volcanic activity in the absence of a dense seismic array, our results suggest that care must be taken when applying ambient seismic noise interferometry in volcanic settings. In a second step, we thus exclude days that show signs of volcanic tremor, reducing the dataset to ~three months, and perform ambient seismic noise tomography. The resulting two-dimensional Rayleigh wave group velocity maps for 0.1 – 0.9 Hz compare very well with images from previous travel time tomography, both, for the main volcanic structures at low frequencies as well as for smaller features at mid-to-high frequencies – a remarkable observation for the temporally truncated dataset. These robust results suggest that ambient seismic noise tomography in Hawai‘i is suitable 1) to provide a three-dimensional S-wave model

for the volcanoes and 2) to be used for repeated time-sensitive tomography, even though volcanic tremor frequently obscures ambient noise analyses. However, the noise characteristics and the wavefield in Hawai‘i in general remain to be investigated in more detail in order to measure unbiased temporal velocity changes.

TABLE OF CONTENTS

LIST OF FIGURES

CHAPTER 1

INTRODUCTION

Ambient seismic noise interferometry is a passive seismic technique developed relatively recently to gain information about the subsurface (e.g. Shapiro & Campillo, 2004; Sabra et al. 2005a). As opposed to traditional seismic techniques that depend on active seismic sources or earthquakes, ambient seismic noise interferometry makes use of the continuously occurring background noise. Such seismic background noise is predominantly generated by ocean waves (Webb, 1998) creating pressure fields that are converted to seismic waves in the solid Earth (Nishida et al., 2008). The resulting noise is mostly composed of surface waves that are low in amplitude but coherent enough to allow for the extraction of information about the sampled subsurface. Cross-correlation of such noise records from pairs of seismometers is used to extract the coherent parts of the noise and has been shown to converge towards the elastic Green's function – i.e., the ground motion through time as recorded in a seismogram at the one station as if an impulsive source would be located at the second (e.g., Lobkis & Weaver, 2001; Shapiro & Campillo, 2004; Snieder, 2004; Sabra et al. 2005a).

Using such noise cross-correlation functions between pairs of seismometers, there have been two main applications demonstrated to be possible. The first one uses the direct surface wave travel times between the station pairs for imaging the subsurface with ambient seismic noise tomography (Sabra et al. 2005b; Shapiro et al. 2005). The second one investigates the multiply scattered part of the seismic signal which is highly sensitive to changes in seismic velocities – an approach that has been utilized to monitor such changes through time (Sens-Schönfelder & Wegler, 2006; Brenguier et al., 2008a; Brenguier et al., 2008b). Both of these applications have proven particularly useful in volcanic settings. First, ambient seismic noise tomography has the potential of providing high-resolution images of S-wave velocities for very shallow (< 5km) magmatic plumbing systems (e.g., Brenguier et al., 2007). And second, the observation of subtle velocity changes has been related to volcanic activity, often as a precursory behavior of volcanic eruptions (Brenguier et al. 2008b; Duputel et al., 2009).

This dissertation presents the first application of ambient seismic noise interferometry in Hawai‘i. In order to explore its utility for studying the Hawaiian volcanoes, we use a dataset continuously recorded by the permanent seismic network on the Big Island of Hawai‘i between 5/2007 and 12/2009 – an interesting period as volcanic activity caused two distinct volcanic tremor sources to be active, and thus the dataset includes both tremor-bearing and tremor-free times. Since Hawai‘i's most active volcano, Kīlauea, frequently emits volcanic tremor, seismic recordings on the Island of Hawai‘i will habitually include this signal. Therefore, we will first explore to what extent such tremor might affect ambient seismic noise interferometry. And, since

tremor in itself is a useful signal for characterizing volcanic activity, we will additionally address the question whether the standard data processing used in ambient seismic noise interferometry might be helpful in enhancing interpretable volcanic tremor signals. Building upon these results, we next exclude volcanic tremor from our dataset and explore the potential of this compromised dataset to image the volcanic structures with ambient seismic noise tomography. The imaged structures together with the improved understanding of ambient seismic noise interferometry in the presence of volcanic tremor will provide an ideal background for future investigations into studying temporal velocity changes in Hawai‘i.

CHAPTER 2

AMBIENT SEISMIC NOISE INTERFEROMETRY IN HAWAIʻI REVEALS LONG-RANGE OBSERVABILITY OF VOLCANIC TREMOR[1]

2.1 Summary

The use of seismic noise interferometry to retrieve Green's functions and the analysis of volcanic tremor are both useful in studying volcano dynamics. Whereas seismic noise interferometry allows long-range extraction of interpretable signals from a relatively weak noise wavefield, the characterization of volcanic tremor often requires a dense seismic array close to the source. We here show that standard processing of seismic noise interferometry yields volcanic tremor signals observable over large distances exceeding 50 km. Our study comprises 2.5 years of data from the USGS Hawaiian Volcano Observatory short period seismic network. Examining more than 700 station pairs, we find anomalous and temporally coherent signals that obscure the Green's functions. The time windows and frequency bands of these anomalous signals correspond well with the characteristics of previously studied volcanic tremor sources at Puʻu ʻŌʻō and Halemaʻumaʻu craters. We use the derived noise cross-correlation functions to perform a grid-search for source location, confirming that these signals are surface waves originating from the known tremor sources. A grid-search with only distant stations verifies that useful tremor signals can indeed be recovered far from the source. Our results suggest that the specific data processing in seismic noise interferometry – typically used for Green's function retrieval – can aid in the study of both the wavefield and source location of volcanic tremor over large distances. In view of using the derived Green's functions to image heterogeneity and study temporal velocity changes at volcanic regions, however, our results illustrate how care should be taken when contamination by tremor may be present.

1 Published as:

Ballmer, S., C. J. Wolfe, P. G. Okubo, M. M. Haney, and C. H. Thurber (2013), Ambient seismic noise interferometry in Hawaiʻi reveals long-range observability of volcanic tremor, *Geophysical Journal International, 194*, 512-5213, doi:10.1093/gji/ggt112.-

2.2 Introduction

In volcanic settings, seismic noise interferometry has advanced into a powerful technique. Ocean-generated seismic noise occurs continuously and is comprised of surface waves with wavelengths sensitive to the shallow subsurface. These properties allow for two applications of interferometry at volcanoes: continuous monitoring of temporal velocity changes (Sens-Schönfelder & Wegler, 2006) that are often associated with subsurface volcanic activity, including precursory behavior prior to some eruptions (Brenguier et al., 2008b; Duputel et al., 2009), and tomographic imaging of shallow volcanic structure (Brenguier et al., 2007; Masterlark et al., 2010). In order for such results to be reliable, the quality of noise recordings and the data processing applied are critical.

The most fundamental step in noise interferometry is retrieval of Green's functions from noise cross-correlation functions (NCFs) between two receivers (Shapiro & Campillo, 2004; Sabra et al., 2005). Diffuse, isotropic wavefields are required for accurate Green's function retrieval, but these characteristics are typically not present in practice (e.g., Froment et al., 2010). An area of research therefore examines the extent of biases on recovered Green's functions, focusing on two factors. First, ocean-generated noise sources are typically directive and thus non-isotropic (e.g., Yang & Ritzwoller, 2008) – a bias for which corrective methods have been developed (e.g., Roux, 2009; Weaver et al., 2009; Yao & van der Hilst, 2009; Froment et al., 2010; Harmon et al., 2010). Second, transient signals (such as earthquakes, volcanic tremor bursts, or storms), as well as persistent signals from localized sources (such as continuous volcanic tremor or the 26 s microseism described by Shapiro et al. (2006)) act as potential sources of contamination. To reduce the effect of such biasing signals, amplitude is partially or fully disregarded during processing (Bensen et al., 2007) and stacking further de-emphases transients. Despite these processing steps, localized sources can remain a cause of bias. Yanovskaya & Koroleva (2011) demonstrated how earthquakes can act as a source of bias, and Harmon et al. (2012) identified temporary effects of storm-generated infragravity waves. The results of Groos et al. (2012) suggest that such signals can be efficiently amplified in NCFs when they persist over longer time windows – results that emphasize the need for more research on the influence of biasing signals on Green's function recovery.

In volcanic settings such as Hawai‘i, volcanic tremor is often an important seismic source. While it may potentially contaminate Green's functions, its study also provides information on volcanic systems. In particular, volcanic tremor is useful for monitoring the volcano plumbing system, as it can be associated with magma movement and degassing (Chouet, 1996). The characterization of volcanic tremor source behavior and wave propagation is therefore a field of interest on its own.

In order to reveal information on tremor's precise location, broadband spectral character, amplitude variations, and mechanism, near-source, small-aperture seismic arrays and specialized

array analyses have often been employed (e.g., Goldstein & Chouet, 1994; Almendros et al., 1997; Konstantinou & Schlindwein, 2003). However, seismic networks typically have large station spacing designed for traditional earthquake studies. In order to use network data for volcanic tremor characterization, techniques are needed that allow the extraction of interpretable tremor signals over large distances. Such prior techniques applied include 1) the use of very low frequencies, where path effects do not deteriorate coherence (Haney (2010), studying Okmok volcano) and 2) the examination of amplitude decay with distance not requiring waveform coherence (Battaglia & Aki (2003) and Battaglia et al. (2005), studying Piton de la Fournaise volcano).

Seismic networks with large interstation distances are commonly used in noise interferometry (even spanning across ocean basins (Lin et al., 2006)), where interpretable signals are extracted from a relatively weak noise wavefield. This technique has also been applied by Shapiro et al. (2006) to study the localized source for a 26 s microseism. These authors applied the standard data processing of noise interferometry to find inter-station arrivals of the 26 s signal on subsets of global networks and used these arrivals to locate the source regions. Similar to Shapiro et al. (2006), we here apply seismic noise interferometry to study another type of localized noise source: volcanic tremor recorded across an island-wide seismic network.

The Island of Hawai‘i with active Kīlauea volcano provides an ideal setting to investigate the performance of noise interferometry in the presence of volcanic tremor. During our 2.5-year-long study period from May 1 2007 to December 31 2009, there were two distinct tremor sources at Kīlauea: first, at Puʻu ʻŌʻō crater complex in Kīlauea’s East Rift Zone and later at Halemaʻumaʻu crater within Kīlauea’s summit caldera. This unique dataset allows us to address the following questions. (1) To what extent does volcanic tremor contaminate estimated Green’s functions? (2) Does the standard data processing to recover Green’s functions also extract volcanic tremor signals that are interpretable over large distances? We first review characteristics of tremor signals and ambient seismic noise recorded in Hawai‘i. We then present reconstructed Green’s functions with focus on characteristics during time periods both with and without volcanic tremor. We further investigate if the retrieved signals in NCFs can help characterize the tremor wavefield and source location.

2.3 Seismic recordings on the Island of Hawai‘i

2.3.1 Seismic network

On the Island of Hawai‘i, the U.S. Geological Survey (USGS) Hawaiian Volcano Observatory (HVO) operates a permanent seismic network. Over 50 stations are distributed in a short-period network across the island (Nakata, 2007) (Figure 2.1) and a closely spaced (5-km aperture)

broadband network is located at Kīlauea's summit region (Dawson et al., 1998). Most of the short period stations are equipped with single-component, vertical-only seismometers with a natural frequency of 1 Hz (about 20% of the stations are 3-component during our study period, although additional stations have been subsequently upgraded to 3-component). We only use data recorded with the short period sensors (see Appendix A for details on data recording and issues causing about 5% of the data to be corrupted). Although the small-aperture summit broadband network is favorable for volcanic tremor study using raw seismogram data, the spatial extent of the short period network (spanning >90 km distance from Kīlauea) is most appropriate for investigating long-range effects of volcanic tremor on Green's functions, and for simplicity we avoid mixing different networks with differing instrument responses.

2.3.2 Ambient seismic noise

Seismic noise is a continuous phenomenon primarily generated by ocean waves. Noise spectra display a dominant microseismic peak at around 0.2 Hz (Webb, 1998). About this spectral peak, energy decreases moderately towards higher frequencies and sharply towards lower frequencies (Webb, 1998). Figure 2.2 shows spectrograms for three short-period stations on Hawai‘i, the locations of which are shown in Figure 2.1 (note that no instrument response correction has been applied and that the short-period instrument response rolls off below 1 Hz; the rapid amplitude decay below 0.2 Hz is partly due to this rolloff). The spectrograms all display noise peaks at ~ 0.25 Hz throughout the 2.5 year time period, with more energetic and broader peaks in winter than in summer. This seasonal variability is likely caused by ocean swells that are more energetic in winter than in summer due to the generating storms being located predominantly in the northern hemisphere (closer to Hawai‘i) during boreal winter and in the southern hemisphere (farther from Hawai‘i) during boreal summer (e.g., Willis et al., 2004; Yang & Ritzwoller, 2008). Such a seasonal difference in source location introduces directivity to the seismic noise field. Despite this directivity, the spectral characteristics around the 0.25 Hz peak as described above are similar for all stations on the Island of Hawai‘i, which is key in reconstructing Green's functions from pairs of receivers (section 2.4).

2.3.3 Volcanic tremor from Kīlauea volcano, Hawai‘i, 2007-2009

Our study period (May 1, 2007 to December 31, 2009) is dominated by activity associated with the Puʻu ʻŌʻō-Kupaianaha eruption in Kīlauea's East Rift Zone, which has been ongoing since 1983 (e.g., Heliker et al., 2003), as well as by unrest at Halemaʻumaʻu crater at Kīlauea's summit that developed in late 2007 and early 2008 (e.g., Dawson et al., 2010). We can identify two

notable tremor sources in the seismic data and accordingly, we define three time windows of importance.

- Puʻu ʻŌʻō time window: from May to mid-June, 2007, before the Father's Day dike intrusion into Kīlauea's East Rift Zone, when volcanic tremor was attributed to activity at Puʻu ʻŌʻō (see Figure 2.3a).

- Tremor-free time window: from mid-June to end of November 2007, when strong continuous volcanic tremor was not observed (although there were a few episodes of intermittent tremor).

- Halemaʻumaʻu time window: commencing in December 2007, when continuous volcanic tremor levels went up in the vicinity of Halemaʻumaʻu crater and were mainly characterized by frequent tremor bursts after a vent-opening explosion within the crater in March 2008 (Figures 2.3b and c). Tremor levels remained elevated until the end of our study period, but were intermittently interrupted by quiet periods after November 2008 – notably for several weeks in December 2008 and July 2009 (Dawson et al., 2010).

The emitted tremor signals can be further characterized by their spectral content on the short-period network. Stations nearest to the tremor sources show the best record of these signals.

-Station STC at ~2 km distance from the Puʻu ʻŌʻō vent reveals a strong tremor signal above 0.5 Hz with peaks at 0.6 and 0.8 Hz – features that are stable throughout the Puʻu ʻŌʻō time window (see Figure 2.2b; such spectral characteristics were also reported by Matoza et al. (2010) from infrasonic data)

-Station URA at ~2 km distance from Halemaʻumaʻu reveals more prominent spectral peaks during the Halemaʻumaʻu time window. The strongest and narrowest of these peaks gradually shifts from 0.4 up to 0.5 Hz during the first six months of 2008 and quickly decays back to 0.45 Hz, remaining stable thereafter (except for pauses in tremor emission). Slightly weaker and broader peaks additionally exist around 0.8-1 Hz (see Figure 2.2c; these characteristics were also reported by Dawson et al. (2010) and Fee et al. (2010) using broadband seismic investigations and infrasonic data, respectively).

In addition to these dominant spectral peaks, prior studies also observe weaker tremor above 1 Hz (up to 5-10 Hz with a small peak around 3 Hz for Halemaʻumaʻu (Fee et al., 2010), and a broadband component at 0.5-15 Hz for Puʻu ʻŌʻō (Matoza et al., 2010)), but we restrict our analyses to 0.1-0.9 Hz, as typical for Green's functions studies on volcanoes (Brenguier et al., 2007; Masterlark et al., 2010).

Tremor amplitudes vary across the seismic network and are naturally strongest on stations nearest to the tremor source. Thus, the effect on spectra is strongest for stations URA and STC for Halemaʻumaʻu and Puʻu ʻŌʻō tremor, respectively. With increasing distance from the source,

tremor effects on spectra decrease dramatically. At STC, which is at ~16 km distance from Halemaʻumaʻu, only the strongest tremor-associated spectral peaks are well recorded during the Halemaʻumaʻu time window. At URA, separated ~20 km from Puʻu ʻŌʻō, the same tremor spectral content is observed as at STC during the Puʻu ʻŌʻō time window, but with lower amplitude (see Figures 2.2b and c). In contrast, HUA (~65 km from Kīlauea's summit) does not reveal any spectral characteristics of the two tremor signals (Figure 2.2a). Moreover, on the raw seismic waveforms (filtered at 0.1-0.9 Hz), a systematic decay of tremor amplitude can be seen with distance from the source across the entire short period network. While Halemaʻumaʻu tremor bursts are detectable in raw waveforms up to ~30 km from the source (Figure 2.3c), both Puʻu ʻŌʻō and Halemaʻumaʻu continuous tremor are less energetic, further decreasing the range of detectability to <10 km (Figures 2.3a and b, respectively).

2.4 Convergence of noise cross-correlation functions to Green's functions

In order to investigate the effect of volcanic tremor on the reconstruction of ambient noise Green's functions, we process data from the vertical components of all functional short period instruments without removing instrument response, since all seismometers are of the same type. Our data are stored in 12-hr-long time series in SAC format. We synchronize each station's time series by reading in data for all stations of each given 12-hr time window and running the "synchronize" command using the SAC software. We then apply demeaning, band-pass filtering (0.05-0.95 Hz), and decimation from 100 to 10 samples/s. We follow Bensen et al. (2007) in performing temporal normalization (running-absolute-mean normalization using 10 s long data segments), and spectral whitening between 0.1 and 0.9 Hz with a wavelet-shaping filter. Data series of six hours length are then cross-correlated with +/- 250 s lag times, the cross-correlations are divided by the root of the multiplied autocorrelations, and then stacked over a 1-day long time window. We use these 1-day long NCFs as a basis for our analyses and perform further stacking and normalization as appropriate (see captions of Figures 2.4, 2.5 and 2.9).

Given the ~0.25 Hz noise peak observed on all station spectrograms (section 2.2.2), it is not surprising that in the 0.1-0.3 Hz frequency band these NCFs successfully converge to Green's functions. As characteristic of Green's functions, the NCFs show a clear, dispersed surface wave group arrival for both the negative and positive time lags, representing waves that travel from one receiver to the other and vice versa. Successful convergence is further confirmed by the reasonable moveouts of surface wave arrivals, as clearly observed when NCFs are plotted against inter-station distance (Figures 2.5a-c). As exemplified for the two station pairs, URA-STC (Figure 2.4a) and URA-HUA (Figure 2.4b), at 0.1-0.3 Hz the NCFs are generally stable through time and do not display perturbations during tremor time windows. However there are intervals when a puzzling zero time lag arrival is present on all station pairs (Figures 2.4a and b), which we suspect may reflect artifacts from electric noise related to analog data telemetry and/or

digitization at a common unit at HVO (see supporting information S2), which may be related to low-frequency spectral lines seen in Figure 2.2; this zero lag arrival seems to lose its effect seasonally during energetic microseismic noise periods in winter.

In contrast, at higher frequency bands (0.3-0.5 Hz and 0.5-0.9 Hz), NCFs behave differently and anomalous signals appear during time windows of known tremor. At 0.3-0.5 Hz, appropriately behaving Green's functions emerge at station pair URA-STC during our first two time windows, whereas NCFs are contaminated by signals on one side during the subsequent Haelema'uma'u time window (Figure 2.4c). At 0.5-0.9 Hz (Figure 2.4e), contaminating signals are present during both Puʻu ʻŌʻō and Halemaʻumaʻu tremor intervals. The basic spatial and temporal characteristics of these contaminating signals are the same as for volcanic tremor identified in the raw seismic data (see spectrograms in Figure 2.2). Additionally, the anomalous signals in NCFs during the Puʻu ʻŌʻō time window exhibit different time lag patterns than during the Halemaʻumaʻu time window, consistent with the two different source locations. This consistency between tremor characteristics observed with raw seismic data and the anomalous signal characteristics in NCFs points towards volcanic tremor as the likely cause of NCF contamination.

With this hypothesis in mind, it is noteworthy that these putative tremor signals are also present in NCFs of station pairs with large distance from the tremor sources. Whereas both stations of the URA-STC pair display tremor signals in their individual spectrograms (Figures 2.2b and c), the spectrogram from station HUA, at a distance of >60 km from both Puʻu ʻŌʻō and Halemaʻumaʻu, appear tremor-free (Figure 2.2a). However, NCFs of the station pair URA-HUA (Figures 2.4b, d, and f) contain similar contaminating signals as URA-STC (Figures 2.4a, c, and e), suggesting that weak tremor signals propagate coherently to distant stations in our network.

Anomalous signals in NCFs, that are temporally coherent over each relevant tremor time window (in that the signals are temporally stable for a given station pair), are in fact present on all of the station pairs that we have examined. For the identified time window and frequency band subsets (i.e., at 0.3-0.5 Hz during only the Halemaʻumaʻu time window, and at 0.5-0.9 Hz during both the Puʻu ʻŌʻō and Halemaʻumaʻu time windows), the NCFs of all station pairs plotted against inter-station distance (see Figures 2.5f, g and i) do not show increasing travel time moveouts as found for uncontaminated time windows and frequency bands (see Figures 2.5a-e, and h). This lack of appropriate surface wave moveouts with inter-station distance indicates that the Green's functions of the three subsets (Figures 2.5f, g and i) are obscured by putative tremor signals.

2.5 Tremor localization from cross-correlations

Given our hypothesis that we are recovering volcanic tremor arrivals in the high-frequency NCFs across the entire HVO seismic network, we seek further confirmation by locating the sources of these signals. Due to the shallowness of the tremor source (less than 1 km (Dawson et al., 2010)), we assume predominant surface wave propagation and hence use a lateral propagation model to find the source epicenter. We apply a grid-search method following Shapiro et al. (2006), who localized the source of the 26 s microseism from NCFs. We use constant propagation velocities determined from a linear least-squares regression of the Green's function moveouts in the tremor-free time window (Figures 2.5e and h revealing velocities of 1.3 km/s at 0.3-0.5 Hz and 1.2 km/s at 0.5-0.9 Hz, respectively).

The localization is performed as follows. We construct a 0.05 degree-spaced geographical grid, each point of which we assume represents a potential source. For each point, we calculate the expected lag time for a given station pair (see Figure 2.6). Because the putative tremor arrivals are affected by scattering, dispersion, heterogeneous velocity structure as well as superimposed Green's functions, we slice a window in the NCFs at +/- 10 s around the expected lag time. We convert amplitudes to absolute values, sum the sliced time series, and stack the results from all station pairs. In order to study the two different tremor sources in differing frequency bands, we repeat this procedure for separate datasets following the subsets presented in section 2.3: a) in the Puʻu ʻŌʻō time window at 0.5-0.9 Hz; b) in the Halemaʻumaʻu time window at 0.3-0.5 Hz; c) in the Halemaʻumaʻu time window at 0.5-0.9 Hz. The NCFs used for these three time windows are the same 40-day stacks shown as envelopes in Figures 2.5f, g and i. We generate three maps (Figures 2.7a, b and c), where highest probable source location is associated with highest amplitude.

The spatial distribution of summed stacked amplitude reveals that the regions of probable source locations are distinct for the two tremor time windows. In the Puʻu ʻŌʻō time window at 0.5-0.9 Hz, the source localizes in Kīlauea's East Rift Zone, where the Puʻu ʻŌʻō crater complex is located. In the Halemaʻumaʻu time window at both 0.3-0.5 Hz and 0.5-0.9 Hz the source localizes in Kīlauea's summit region, where Halemaʻumaʻu crater is located. Although the source location in the Puʻu ʻŌʻō time window is less well constrained than in the Halemaʻumaʻu time window, both results indicate two separate source regions – a finding that also holds true when tracking the source location through time for our entire study period (see movie[2] in digital supplemental material for grid search in the 0.5-0.9 Hz band, performed in 5-day intervals, covering 2007 May 1 to 2009 December 31). An artificial localization in these regions (e.g., due to station configuration) can be ruled out when considering the results obtained from the tremor-

2 The movie on tremor localization is also available online as supporting information for the article Ballmer et al. (2013) at: http://gji.oxfordjournals.org/lookup/supp1/doi:10.1093/gji/ggt112/-DC1

free time window (Figure 2.8). Although our approach does not yield a high-precision location, the results agree well with our hypothesis that volcanic tremor contaminates the NCFs.

The existence of tremor signals is further revealed by examining NCFs in the reference frame for a localized tremor source. Instead of plotting the NCFs against inter-station distance (as in Figure 2.5), Figure 2.9 references the differential distance between the tremor source (as determined by the localizations) and each of the two stations. The results display single linear trends of arrivals that are in accordance with the constant surface wave velocities determined from Green's function moveouts (Figures 2.5e and h). Note that we fail to reconstruct such a single linear trend of arrivals versus differential distance for Green's functions in the tremor-free time window (Figure 2.8b): instead, a cross-like pattern is recovered composed of two linear trends with opposite sign of slope.

In order to investigate how useful distant stations are for localizing the tremor source, we repeat the grid-search after removing stations according to some minimum distance cutoff from a tremor source We perform a source localization using 30 km, 40 km or 50 km as minimum cutoff distance (Figures 2.7d-l). Results in the Halemaʻumaʻu time window are similar to the original localization using all stations (compare Figures 2.7b-c with Figures 2.7e-f, h-i, k-l). However, localization quality decreases with increasing cutoff distance (i.e., with fewer station pairs). In the Puʻu ʻŌʻō time window the pattern obtained for a cutoff of 30 km also agrees well with the original localization (compare Figure 2.7a with Figure 2.7d). But for cutoffs of 40 km (Figure 2.7g), and particularly for 50 km (Figure 2.7j), the pattern shows more pronounced deviation. Weaker tremor levels in the Puʻu ʻŌʻō time window (see Figure 2.2) probably cause a faster decay in the quality of tremor arrivals with distance and hence lead to a lower quality localization using more distant stations. Nonetheless, both results demonstrate how NCFs can extract long-range tremor arrivals and highlight their potential for estimating the source location with stations at distances of ~ 30 km and exceeding 50 km, with location quality dependent on source strength and station configuration.

2.6 Discussion

We present the first investigation into whether techniques used for seismic noise interferometry may be applied to the study of volcanic tremor and how such tremor affects estimation of ambient noise Green's functions. Due to our unique dataset that contains two separate tremor sources, we are able to show that noise cross-correlation functions (NCFs) do not always converge to Green's functions when volcanic tremor is present. This result is in accordance with prior findings that Green's functions may be biased due to transient signals such as earthquakes (Yanovskaya & Koroleva, 2011) and storms (Harmon et al., 2012) as well as due to persistent localized signals (Shapiro et al., 2009; Groos et al., 2012). Moreover, we demonstrate how NCFs

extract surface waves from volcanic tremor over large distances that are useful to characterize the source location.

Whereas volcanic tremor in the Puʻu ʻŌʻō and Halemaʻumaʻu time windows is not apparent in the raw data for distances greater than ~10 and ~30 km, respectively, we observe tremor arrivals in the NCFs at much larger distances (i.e., 30 and > 50 km). This result shows that signal coherence at 0.1-0.9 Hz is not distorted by path effects at these large distances. This finding is in general accordance with observations by Haney (2010), who reported tremor signals to be free of path effects at 0.2-0.4 Hz using stations with a maximum distance of ~15 km from the source. The distances of coherent tremor signals in NCFs, however, far exceed observations with raw data. While correlation approaches (and in particular, matched filter analyses) are known to have success in detecting weak coherent signals, we nonetheless find it remarkable how strong tremor arrivals are extracted from initially undetectable tremor signals in the presence of energetic ambient seismic noise that converges to Green's functions in certain frequency bands.

Groos et al. (2012) provide an explanation for the amplification of weak signals such as tremor with seismic interferometry. They found that cross-correlation after spectral whitening for short window lengths of <12 hrs with subsequent stacking can enhance signals of persistent localized sources. After spectral amplitudes are discarded, temporal and spatial stability of initially very small signals ensure reliable emergence in cross-correlations using short windows, whereas the emergence of Green's functions is not efficient without signal averaging (as obtained through correlations using long windows and/or stacking). Our results obtained with 6-hr-long time windows illustrate in practice how strong the signal amplification can be. Note that Shapiro et al. (2006) used sign bit normalization in their study of the 26 s microseism, suggesting that generally both the one bit as well as running absolute mean normalizations are suitable to amplify persistent localized sources. However, as one bit normalization strongly distorts the waveforms and has been suggested to negatively influence broad-band signals (Sabra et al., 2005; Groos et al., 2012) the running absolute mean normalization might be more effective for analyses of volcanic tremor with broad frequency content. More systematic study on the effects of differing processing steps on persistent localized sources with various characteristics would help in tuning the processing for more targeted amplification or suppression of such signals.

We note that many of the world's volcanoes lack a dense seismic network, such as for various volcanoes in the Aleutians (Neal et al., 2011) or in South America (Siebert & Simkin, 2002-), so the ability to extract volcanic tremor signals over very large distances may provide new research opportunities. Our results suggest that seismic noise interferometry is generally applicable to volcanic tremor, since Puʻu ʻŌʻō and Halemaʻumaʻu tremor both produce excellent signals in NCFs despite their very different generation mechanisms and waveform character (see Matoza et al., 2010 for Puʻu ʻŌʻō, and Chouet et al., 2010 and Fee et al., 2010 for Halemaʻumaʻu). Our localization results are consistent with prior studies, which found that the Halemaʻumaʻu source

is located underneath the northeastern crater rim (Dawson et al., 2010) and that the Puʻu ʻŌʻō source is likely to be distributed and not originating from a single vent (Matoza et al., 2010). Our network-based localization results are less accurate than prior, array-based studies of these tremor sources, particularly when we only use distant stations. Nonetheless, the approach presented in our paper may be a useful tool for cases, where only sparse station coverage is available. The distance at which interpretable tremor signals can be extracted is much larger than for array methods and even than for prior approaches specifically developed for sparse seismic networks, such as mapping tremor's amplitude decay with distance (e.g., Battaglia et al., 2005).

Long-range volcanic tremor signals in NCFs contaminate Green's functions for purposes of monitoring temporal velocity changes or tomographic imaging at Kīlauea, highlighting how Green's functions estimates may be prone to bias in volcanic settings. However, despite such contamination, these Green's functions might still be useful for monitoring temporal velocity changes given that the sources are spatially stable (Hadziioannou et al., 2009) and information for tomography might be extracted using the method of Roux (2009) for directive noise. We demonstrate how recovered tremor signals can be used to monitor the source location through time (see movie S1) and hence provide a means to assess spatial source stability to ensure quality of temporal change measurements. Finally, for tomographic imaging in volcanic settings quality control of Green's functions seems to require careful examination of NCFs to ensure that tremor is not a source of contamination.

2.7 Conclusions

We demonstrate that interpretable tremor signals can be observed over large distances after applying data processing typically used for Green's function retrieval. Due to our unique dataset that contains volcanic tremor from Puʻu ʻŌʻō and Halemaʻumaʻu craters lasting months and years, respectively, we are able to clearly identify signals in the noise cross-correlation functions that have the same temporal and spectral characteristics as the known tremor. Whereas this result could be anticipated for close-in station pairs with good tremor record in the raw data, it is surprising to find tremor signals in cross-correlations for all station pairs in the network considering that, beyond a certain range, path effects might strongly distort waveform coherence. However, robust results of localizing the tremor source even with only distant stations shows that inter-station arrivals can be extracted with high quality over much larger distances than previously realized – findings that point towards the effective amplification of the tremor signals over the noise. These results highlight the possibility of using seismic network data with large station spacing for tremor monitoring of volcanoes, which might be particularly promising in remote settings. In view of using noise-derived Green's functions to image heterogeneity and study temporal velocity changes, these results also illustrate how care should be taken in volcanic regions even when tremor may seem weak or absent in the raw data.

2.8 Figures

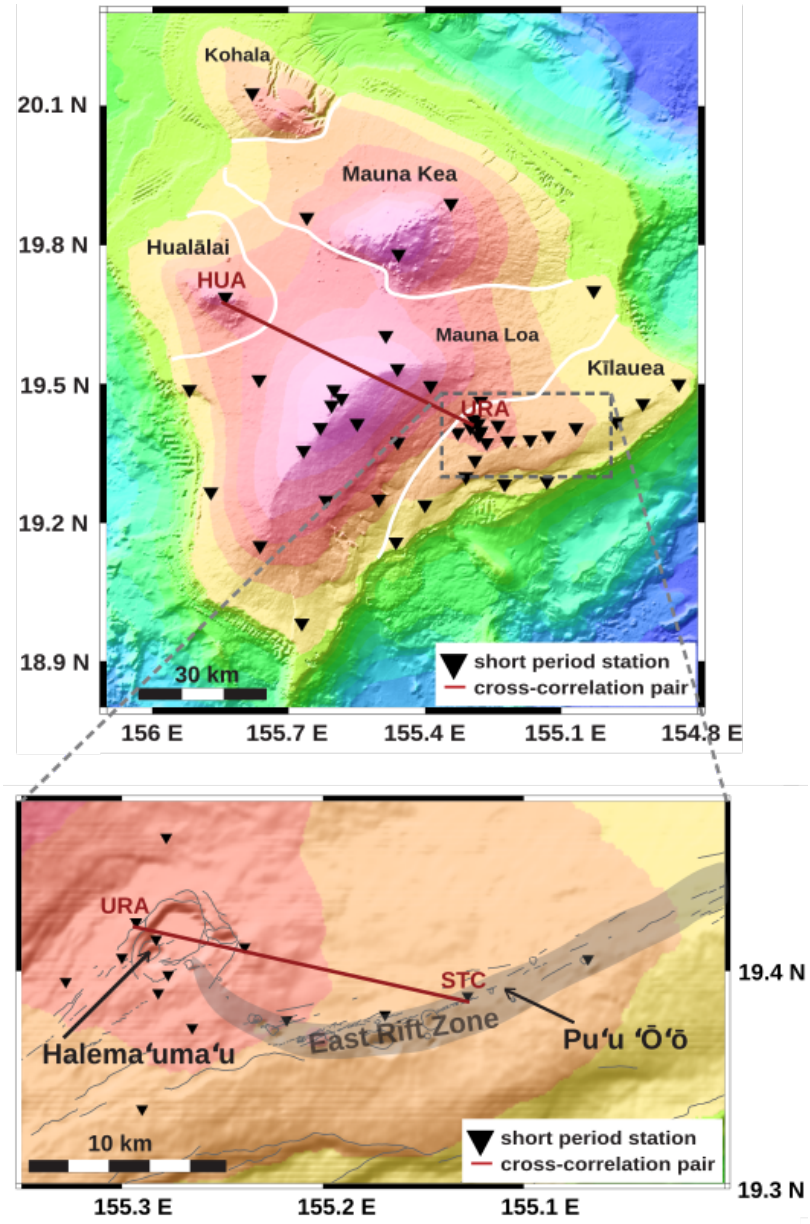

Figure 2.1: Location of the USGS Hawaiian Volcano Observatory short-period seismic network (black triangles), along with topography, volcano boundaries (white lines), and the names of stations for which spectrograms and cross-correlation pairs are later shown. Inset shows Kīlauea summit along with locations of Halemaʻumaʻu and Puʻu ʻŌʻō craters (black arrows), the East Rift Zone (grey shading), and other geologic structures (grey lines).

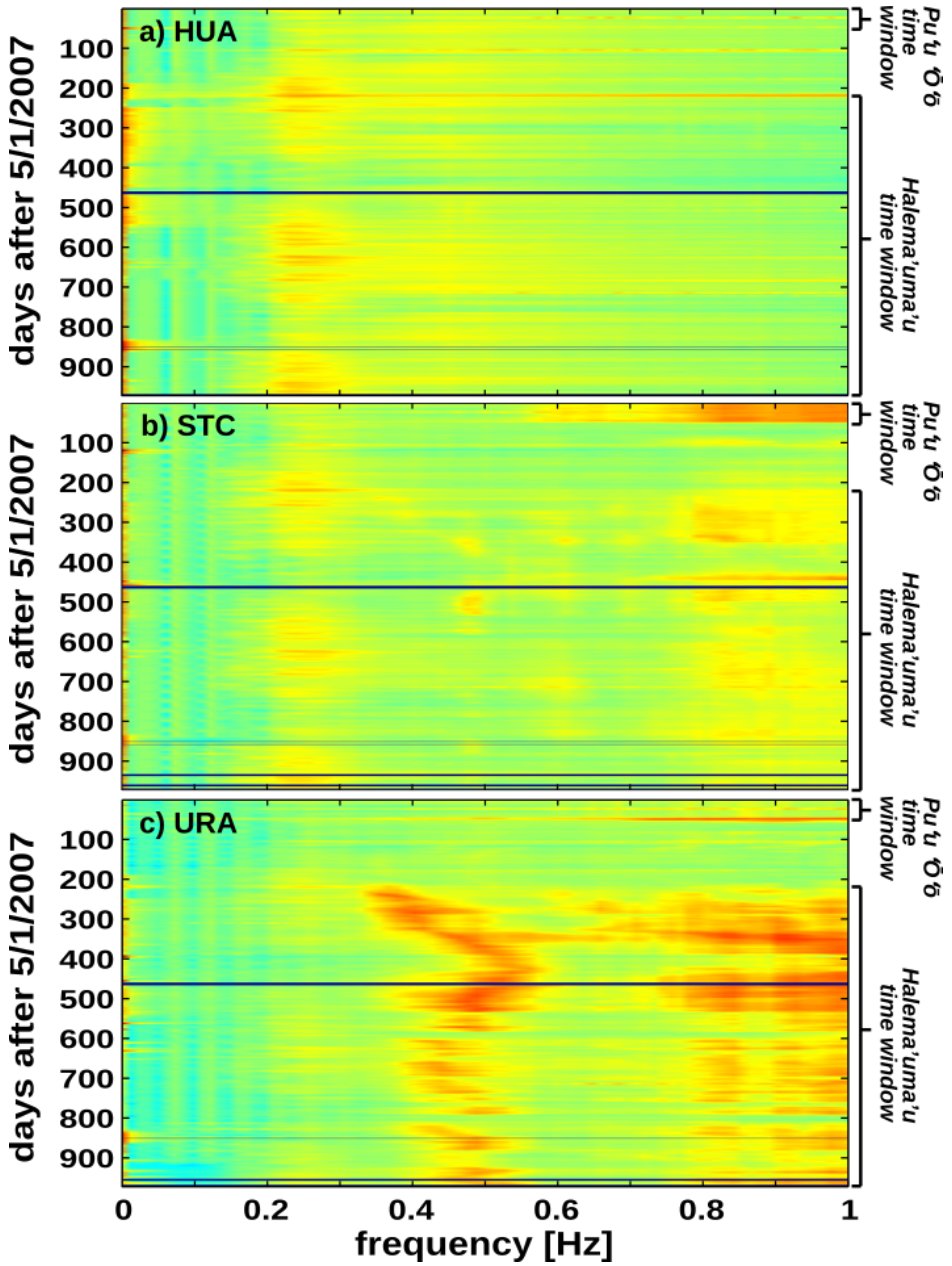

Figure 2.2: Spectrograms for three short period stations (a: HUA, b: STC, c: URA) between 05/01/2007 and 12/31/2009 (averaged over five-day-long moving windows). Note that no instrument response correction has been applied and that the short-period instrument response rolls off below 1 Hz. The rapid amplitude decay below 0.2 Hz is partly due to this rolloff. Signals above ~0.55 Hz in the *Pu'u 'Ō'ō time window* are strongest at station STC and several spectral peaks (~0.35-0.55 Hz, 0.8-0.85 Hz and 0.9-0.95 Hz) in the *Halema'uma'u time window* are strongest at station URA. These signals are attributed to volcanic tremor and are not apparent in the spectrogram of station HUA (>60 km from the tremor sources).

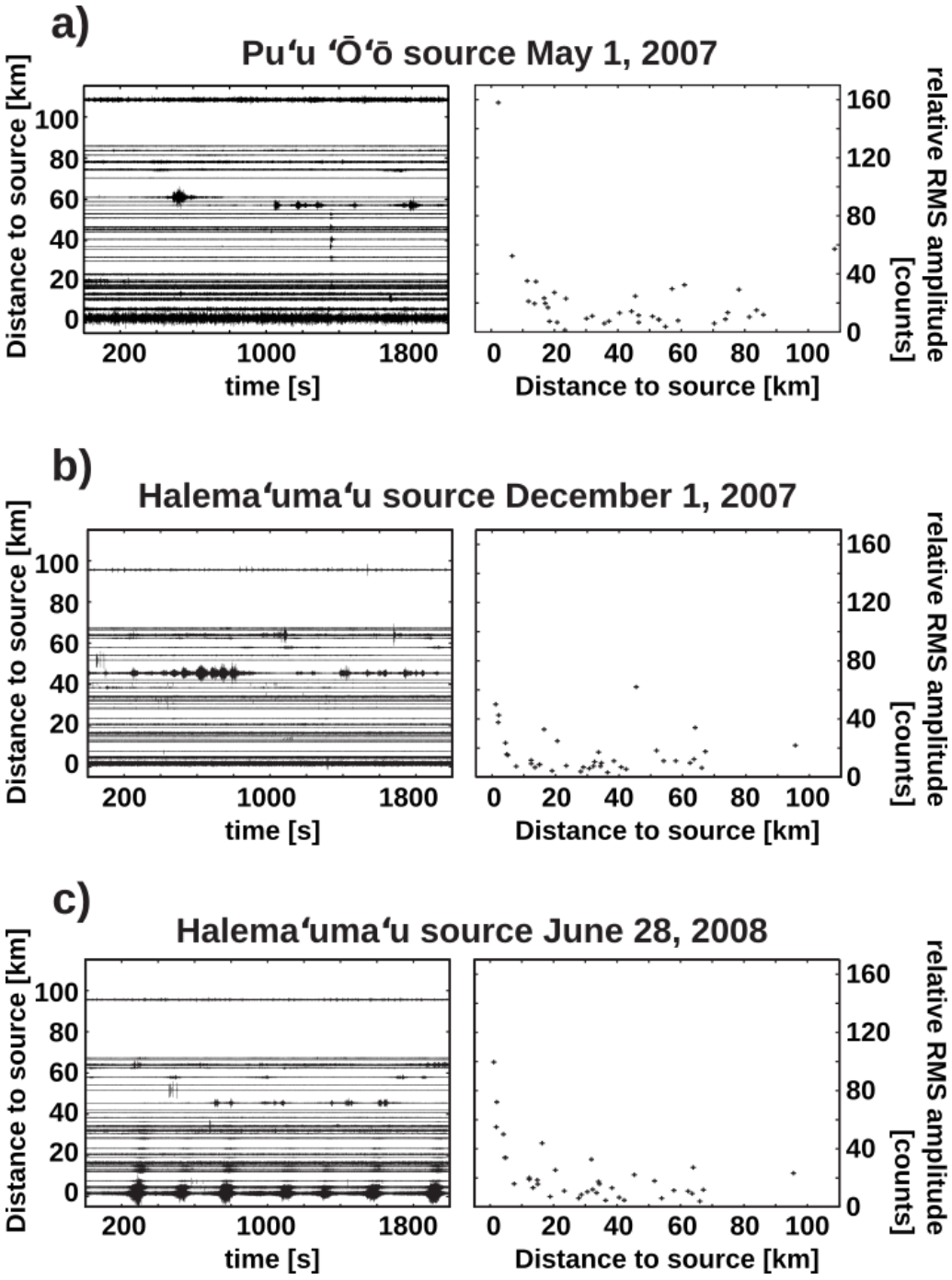

Figure 2.3: Volcanic tremor amplitude variation with distance on (a) May 1, 2007 (continuous Pu‘u ‘Ō‘ō tremor), (b) December 1, 2007 (continuous Halema‘uma‘u tremor), and (c) June 28, 2008 (tremor bursts and continuous tremor from Halema‘uma‘u). Left: waveforms of stations filtered at 0.1-0.9 Hz and ordered by distance from the tremor source. Right: root-mean-square (rms) amplitude versus distance, showing systematic amplitude decay with distance.

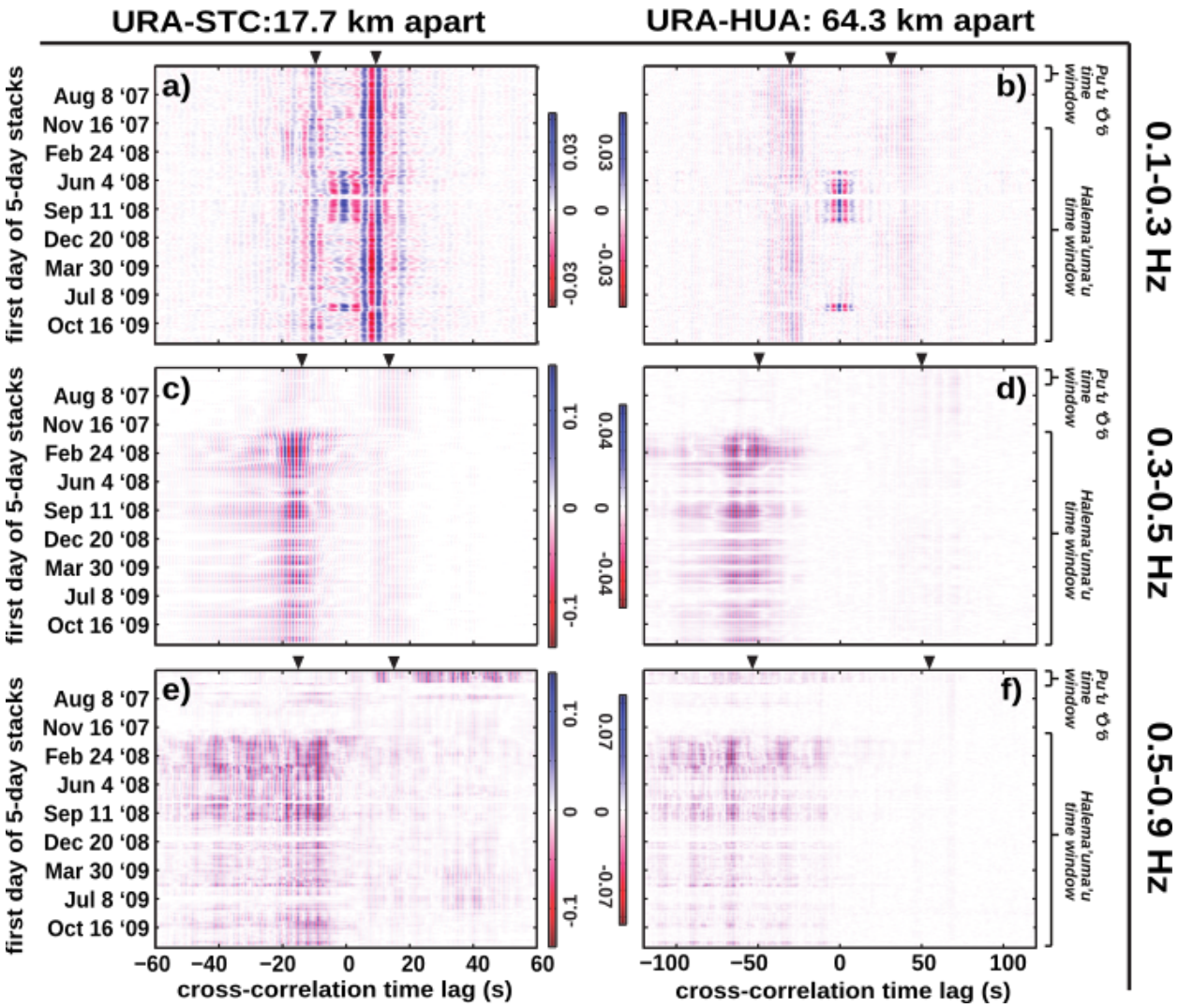

Figure 2.4: Examples of noise cross-correlation functions (NCFs; five-day stacks generated from averaging one-day stacks over a five-day-long moving window) versus time in differing frequency bands for two station pairs (left column: URA-STC; right column: URA-HUA). Black triangles at topside of subfigures indicate the predicted surface wave group arrival times for Green's functions based on velocities determined in Figure 2.5. (a) At 0.1-0.3 Hz, the URA-STC NCFs converge to Green's functions, and signals around +/- 8 s represent direct surface waves. Larger amplitudes of surface wave arrivals at positive lags reflect a directive noise field, consistent with STC being closer to the southeast coastline. (b) Station pair URA-HUA at 0.1-0.3 Hz with direct surface wave arrivals around +/- 35 s. (c-f) Anomalous but temporally coherent signals are observed at 0.3-0.5 Hz (middle row) in the *Halemaʻumaʻu time window*, and at 0.5-0.9 Hz (bottom row) in the *Puʻu ʻŌʻō* and *Halemaʻumaʻu time windows*. See text for discussion of high energy centered at lag time 0 s in subfigures a) and b).

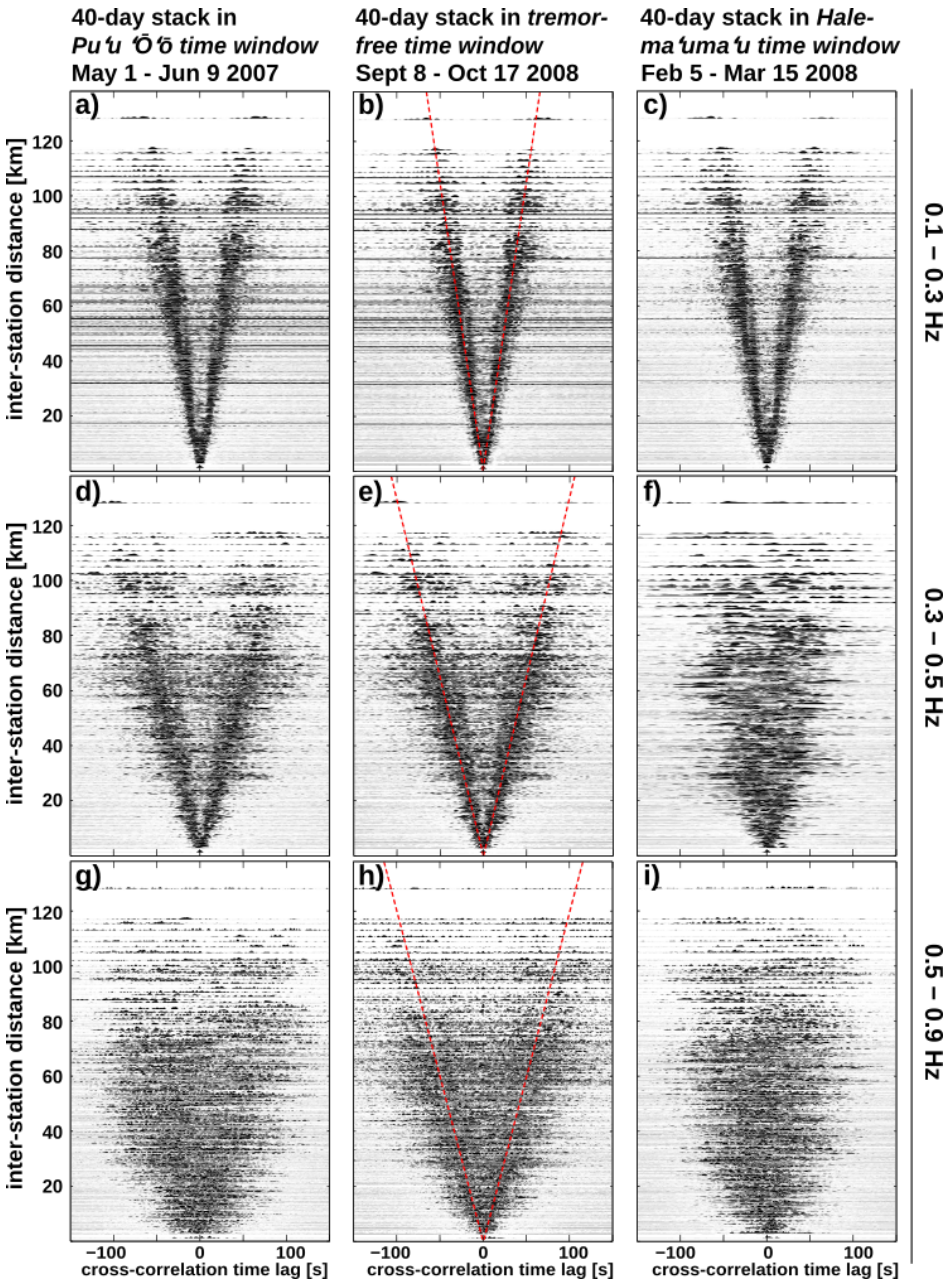

Figure 2.5: Envelopes of noise cross-correlation functions (NCFs) plotted against inter-station distance in three time windows (columns) and two frequency bands (rows). NCFs are stacked over 40 days and amplitudes are normalized. Red dashed lines indicate predicted arrival times based on average group velocities (2.1 km/s at 0.1-0.3 Hz, 1.3 km/s at 0.3-0.5 Hz and 1.2 km/s at 0.5-0.9 Hz), as estimated from linear regressions on moveouts in the *tremor-free time window* (middle column). Note that moveout patterns are distorted and Green's functions are strongly obscured at 0.3-0.5 Hz in the *Halemaʻumaʻu time window* (f) and at 0.5-0.9 Hz in both the *Puʻu ʻŌʻō* and *Halemaʻumaʻu time windows* (g and i, respectively).

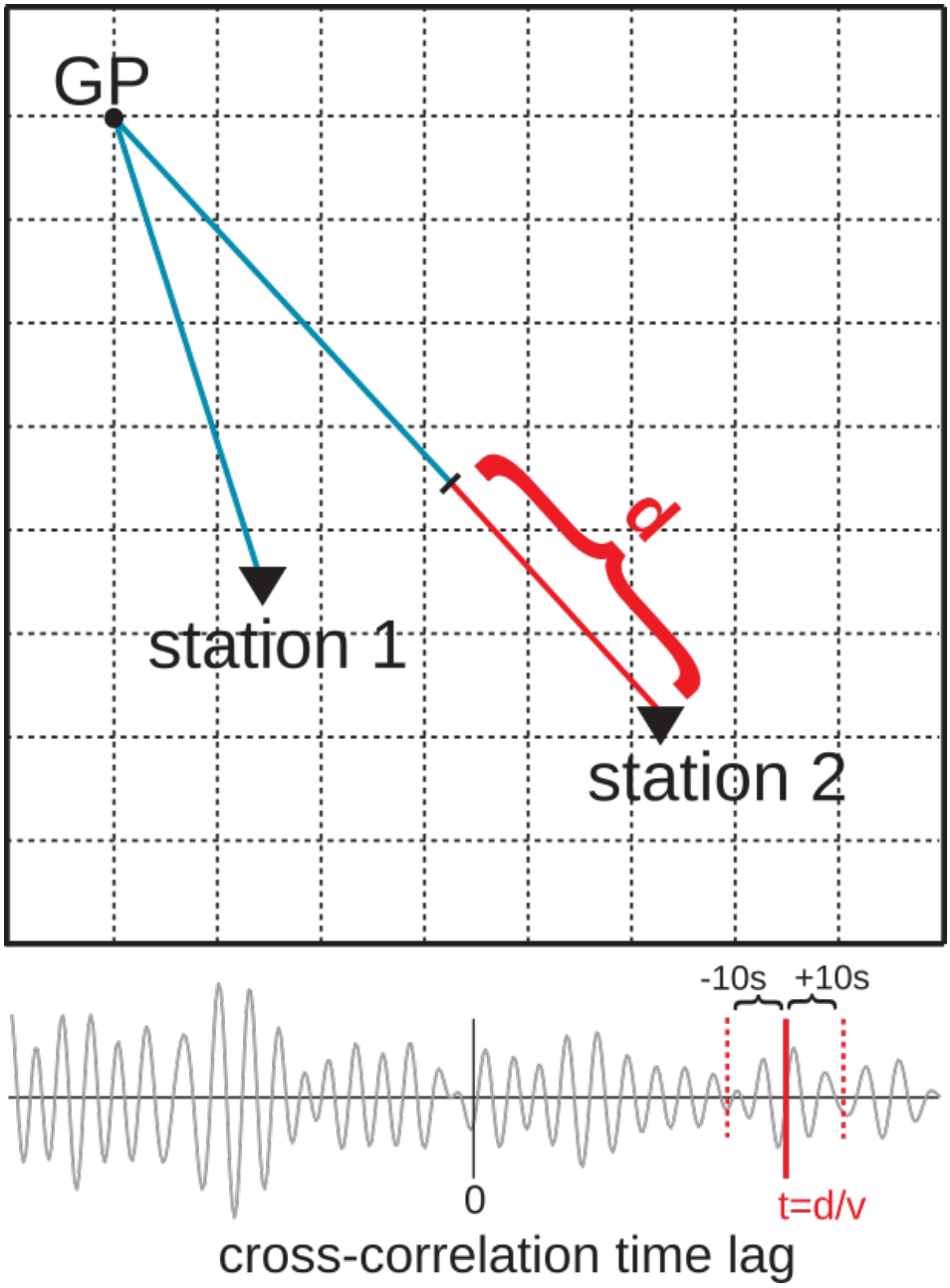

Figure 2.6: Illustration of how summed stacked amplitude is determined for the source localization. Each grid point (*GP*) is treated as a possible source of coherent signals. The differential distance, *d*, between the source and two stations, divided by the wavespeed, *v*, determines the predicted lag time, *t*, of an arrival from the source location. Then, the absolute amplitudes within a time window of +/-10 s around the predicted time are stacked over all possible station pairs and the summed amplitude for each grid point is plotted in map view (Figure 2.7).

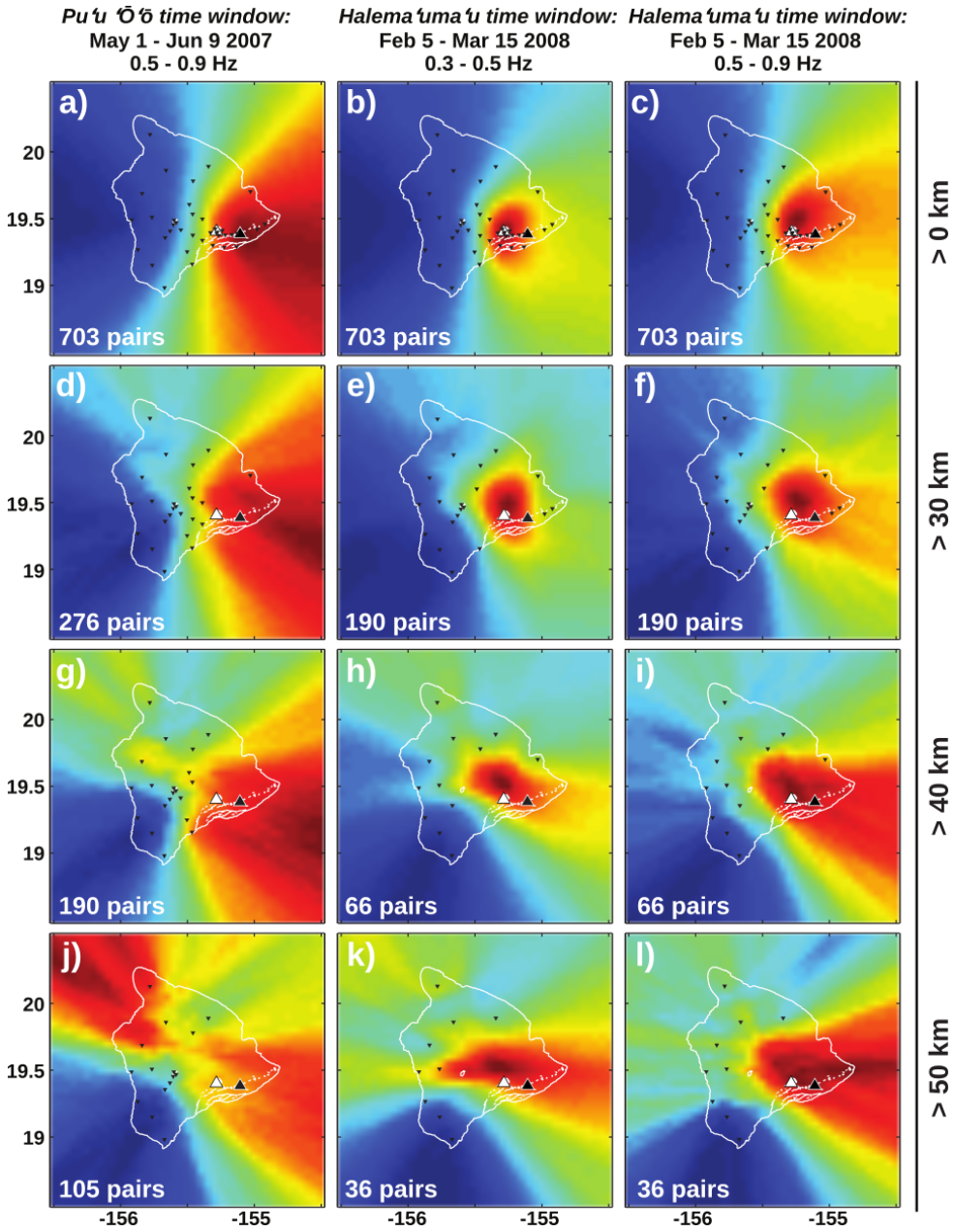

Figure 2.7: Results of grid-search to localize the source of contamination in noise cross-correlation functions (NCFs) during *Pu'u 'Ō'ō* (left column) and *Halema'uma'u time windows* of tremor (middle and right columns). Different station subsets are used: all stations (a-c) and with a minimum cutoff distance to the tremor source of 30 km (d-f), 40 km (g-i), and 50 km (j-l). Stations used are shown by inverted black triangles. The two larger triangles indicate locations of Pu'u 'Ō'ō (black) and Halema'uma'u (white). White lines outline the coast and geographic features. For each hypothetical source location, the summed stacked amplitudes of the station pairs' NCFs are plotted, with dark red colors indicating more probable source locations.

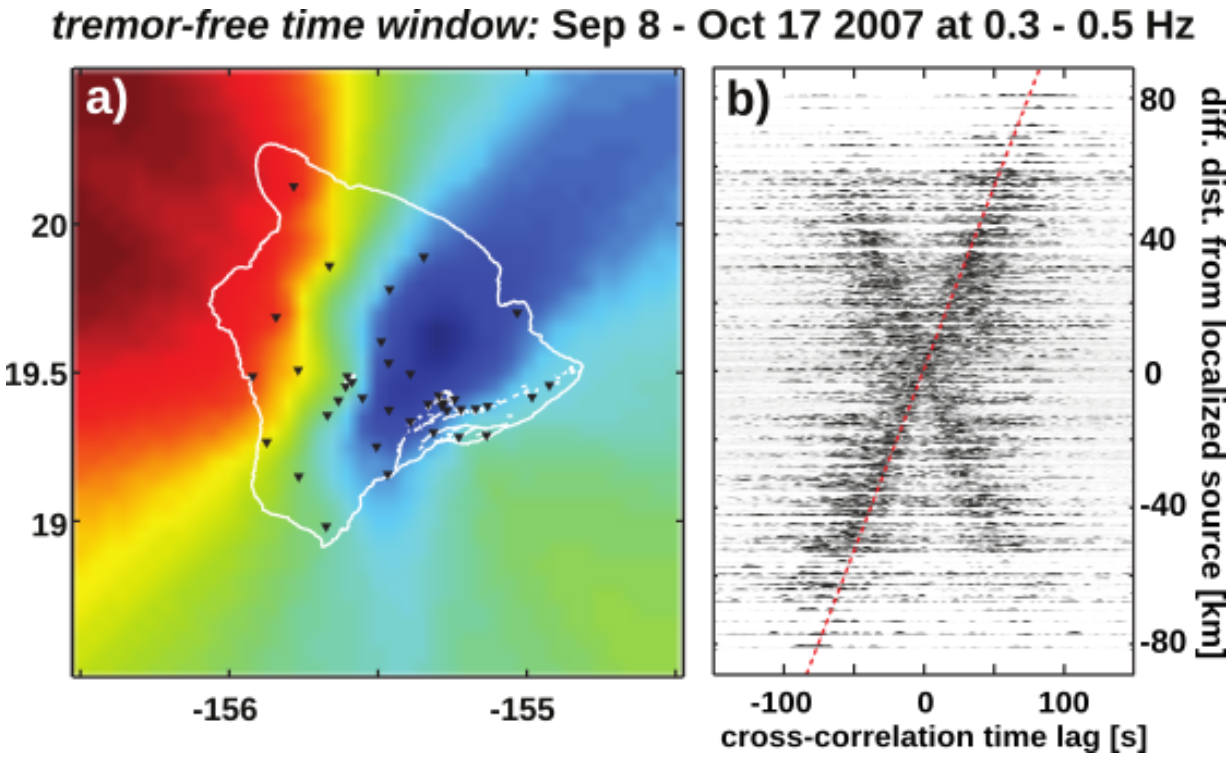

Figure 2.8: (a) Localization and (b) envelopes of noise cross-correlation functions (NCFs) plotted against differential distance of the station pair to the localized apparent source in the *tremor-free time window* at 0.3-0.5 Hz. Stations are shown by inverted black triangles in a). Note that the amplitude distribution in a) does not represent predominant source region of microseism noise. The red dashed line in b) indicates predicted lag times for arrivals from the solution for the apparent source. Note that a cross-like pattern composed of two linear trends in b) results from plotting the uncontaminated NCFs (Green's functions) that show moveout with inter-station distance in Figure 2.5e in a different order (against differential distance to an apparent source).

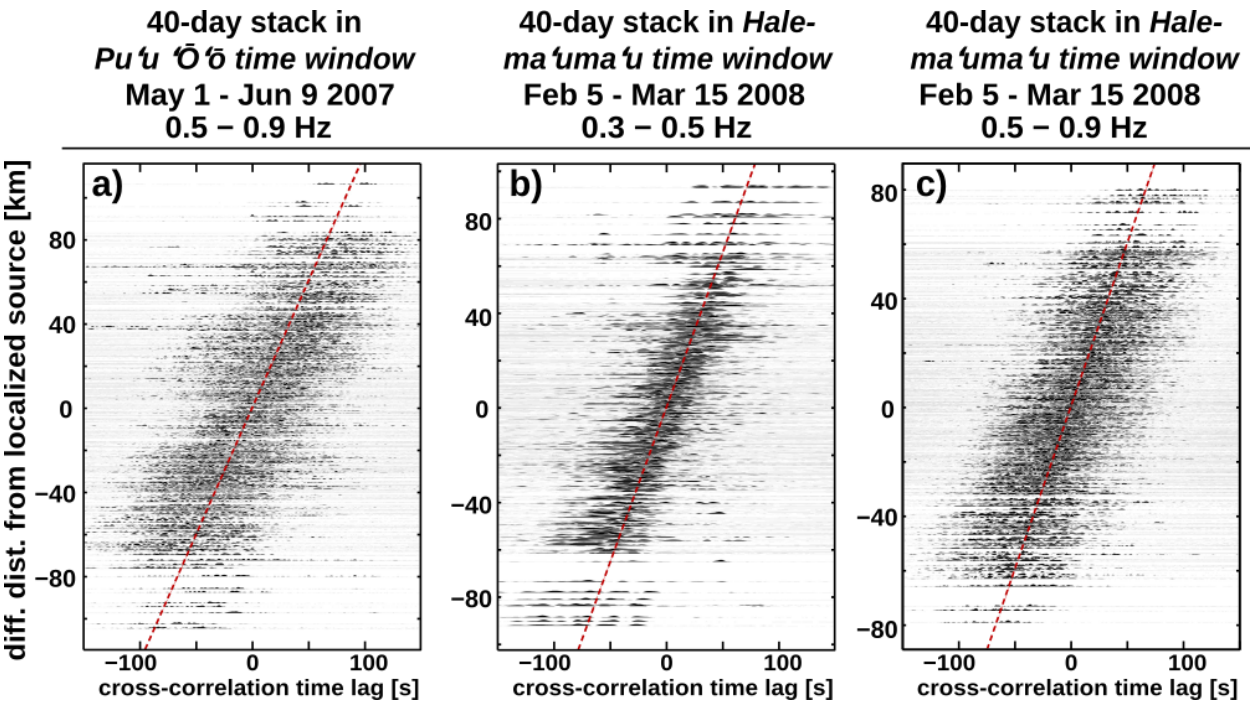

Figure 2.9: Envelopes of noise cross-correlation functions (NCFs) plotted against differential distance of the station pair to the tremor source (as determined by localization (Figures 2.7 a-c)). NCFs are stacked over 40 days and amplitudes are normalized. Note that high amplitude arrivals in the NCFs show single linear trends that match predicted lag times (red dashed lines) for waves originating from the tremor sources traveling with surface wave group velocities as determined in Figure 2.5.

CHAPTER 3

SHORT-PERIOD RAYLEIGH WAVE GROUP VELOCITY MAPS FOR HAWAIʻI ISLAND, FROM AMBIENT SEISMIC NOISE[3]

3.1 Summary

Ambient seismic noise tomography has proven efficient to image volcanic structures. Local conditions like station configuration and the quality of dispersion measurements attainable determine how well this technique performs in a given setting. Here, we have performed ambient seismic noise tomography for the Island of Hawai‘i for the first time. After rejecting daily noise cross-correlation functions that show signs of volcanic tremor contamination, the dataset was reduced from ~2.5 years to ~3 months. Dispersion measurements of fundamental mode Rayleigh waves were performed from 0.1 – 0.9 Hz. We found a gradual decrease of acceptable measurements toward higher frequencies and, after additional quality control, two frequency bands with an unexpectedly high number of inconsistent measurements stand out (0.24 to 0.36 Hz and also to some extent at 0.64 to 0.78 Hz). Using a linearized inversion, we obtained robust 2D fundamental-mode Rayleigh wave group velocity maps with highest resolution in the low- to mid-frequency band around Kīlauea and Mauna Loa volcanoes. The resulting velocity anomaly patterns agree well with previous earthquake-based tomography studies. This pilot study demonstrates the high potential of noise tomography for imaging the subsurface structures of Hawaiian volcanoes.

3 In preparation for publication:
Ballmer, S., R. A. Dunn, M. M. Haney, C. J. Wolfe, P. G. Okubo, and C. H. Thurber, Short-period Rayleigh wave group velocity maps for Hawai‘i Island from ambient seismic noise, *in preparation.*

3.2 Introduction

Determining the internal structure of active volcanoes is key to understanding processes such as edifice construction, magmatic plumbing, eruption timing and dynamics, or the chemical evolution of magmas. A primary means for imaging the subsurface is via seismic methods, and ambient seismic noise tomography (ASNT) is a passive imaging technique that can provide constraints on shallow structures. In this method ambient noise time series, recorded at two distant receivers, are used to calculate noise cross-correlation functions (NCFs) that converge to the elastic Green's function: the inter-station impulse response that would result if an impulse source located at one receiver was recorded at the other (e.g., Sabra et al., 2005a; Shapiro and Campillo, 2004). Surface wave dispersion curves (phase or group velocity versus frequency) can then be extracted from the NCFs, providing station-to-station travel times suitable for surface wave tomography (e.g., Sabra et al., 2005b; Shapiro et al., 2005).

The tomographic image is constructed by inverting travel time information from all available station-to-station propagation paths for two-dimensional velocity maps at different frequencies. Since propagation paths are determined by the location of the station pairs, lateral resolution depends largely on station geometry, while the penetration depth of a surface wave is proportional to its wavelength, and thus depth information depends largely on the frequency bands used. Hence, while long period data samples deeper, ASNT with short-period data (where surface wave energy in ambient noise is strongest (Webb, 1998)) can potentially provide high-resolution images of the uppermost ~10km of the subsurface. The resulting phase or group velocity tomographic models can be used to determine S-wave velocity (V_s) structure. Since V_s is sensitive to fluid-bearing material (e.g., Hansen et al., 2004; Lees, 2007), ASNT is particularly promising in complementing local earthquake tomography in imaging shallow volcanic systems.

Short-period ASNT has already proven useful to image features associated with shallow magmatic plumbing systems at a variety of volcanoes, including Piton de la Fournaise, La Reunion (Brenguier et al., 2007; Mordret et al., 2015), Okmok volcano, Alaska (Masterlark et al., 2010), Lake Toba caldera, Sumatra, Indonesia (Stankiewicz et al., 2010; Jaxybulatov et al., 2014), Ulturuncu Volcano, Bolivia (Jay et al., 2012), Mt Asama, Japan (Nagaoka et al., 2012), Colima Volcano, Mexico (Spica et al., 2014), Lazufre Volcanic Area, Chile/Argentina (Spica et al., 2015), and Naruko/Onikobe volcanic area, Japan (Tamura and Okada, 2016). However, the performance of ASNT varies from setting to setting due to network constraints (i.e., station configuration, instrument type and recording time) and regional conditions. The noise source distribution and its variability through time at different frequencies are regionally-varying properties of the ambient noise field that fundamentally impact the quality of Green's functions recovery (e.g., Yang & Ritzwoller, 2008; Yao & van der Hilst., 2009; Froment et al., 2010). Hence, examination of the regional ambient noise properties and its influence on Green's

function recovery is necessary in order to characterize the performance capabilities of ASNT in a given setting.

Here, we conduct the first ASNT study for the Island of Hawai‘i and evaluate ASNT performance at short periods under the given regional conditions. Our prior work (Ballmer et al., 2013; see chapter 2) revealed that NCFs in Hawai‘i are often contaminated by volcanic tremor at considerable distance from the source, making certain time windows unusable for surface wave dispersion measurements. These findings question performance of ASNT in Hawai‘i, and thus motivate an investigation of the suitability to image the Hawaiian volcanoes with this technique. Using data from the USGS Hawaiian Volcano Observatory (HVO) short period seismic network (see Figure 3.1) we calculate NCFs and remove tremor-bearing time windows. The remaining NCFs are used for surface wave dispersion measurements that are inverted for Rayleigh wave group velocity maps at high frequencies. We then compare our results with known structures previously imaged with body wave tomography, allowing us to assess current limitations and possible improvements for ASNT in Hawai‘i.

3.3 Previous seismic tomography studies

Several earthquake and active source seismic tomography studies carried out on a regional scale have revealed the main volcanic structures of Kīlauea and Mauna Loa (e.g., Okubo et al., 1997; Monteiller et al., 2005; Park et al., 2007; Got et al., 2008; Park et al., 2009; Lin et al., 2014a), the two active volcanoes on the Island of Hawai‘i (see Figure 3.1 for volcanoes' location as well as location of geologic features). Low V_p anomalies are characteristic for the Hilina fault zone in Kīlauea's south flank and around the Kaoiki fault zone between Kīlauea and Mauna Loa – areas that are associated with volcaniclastic sediments and hyaloclastites. In contrast, high V_p anomalies are present beneath Kīlauea's summit and upper rift zones, as well as Mauna Loa's summit and upper southeast flank. These anomalies are interpreted as the dense volcanic cores indicative of persistent magma pathways that are mainly composed of solidified, uncracked magmatic cumulates.

Plumbing structures are roughly outlined in regional models, but greater detail is provided by more targeted studies. In particular, better ray coverage in some studies, as well as improved tomography techniques in others have allowed higher resolution imaging of Kīlauea's central features. For example, the outline of Kīlauea's magma transfer complex, represented by high V_p in the summit area below ~4 km depth, has been refined with double difference tomography (Monteiller et al., 2005). Instead of one broad V_p anomaly (e.g., Thurber, 1984; Okubo et al., 1997) the refined model reveals three connected segments: one shallow anomaly located below the upper east rift zone, and two distinct anomalies located below the caldera rim to the south and southwest that protrude down to ~9 km. The lack of sufficient ray coverage in the summit

area, however, did not allow this study to resolve structure at depth <4 km. In contrast, Dawson et al. (1999) employed additional stations in the summit area. The resulting improved resolution at depths <4 km provided evidence for an active magma storage zone as indicated by low V_p values below the southern caldera / upper east rift zone, a feature that had also been observed by Thurber (1984) and Rowan & Clayton (1993). Likewise, Haslinger et al. (2001) employed a temporary array in the east rift zone, an experiment targeted at finding a possible deep magma body. A sizeable low V_p anomaly at 9 km depth seemed to provide evidence for such a feature.

Knowledge of S-wave velocities (V_s) in addition to V_p, however, is critical in order to unambiguously identify fluid-bearing material. A high V_p/V_s ratio in addition to generally low V_p and V_s is a widely used indicator to identify active magma reservoirs. In Hawai‘i, four studies have addressed V_p/V_s. First, Dawson et al. (1999) focused on Kīlauea’s summit and imaged high V_p/V_s values at shallow depth below the caldera confirming the existence of a magma reservoir in that area as proposed by earlier V_p studies (Thurber, 1984; Rowan & Clayton, 1993). The extent of this high V_p/V_s zone also revealed that partial melts in the magma reservoir are likely distributed within two distinct zones instead of one. These two zones coincide with the broader low V_p volume, which may represent a broader region of high temperatures. The next two V_p/V_s models (Hansen et al., 2004, and Lin et al., 2014b) targeted the hypothesized deep magma body in the east rift zone (Haslinger et al., 2001). Hansen et al. (2004) did not find elevated V_p/V_s ratios in that area, and concluded that the low V_p anomaly at 7 km depth located beneath the central east rift zone might be caused by a trapped CO_2-reservoir. In contrast, Lin et al. (2014b) revealed a zone of high V_p/V_s ratios at 9 km depth beneath the upper east rift zone that coincides with low velocities in both V_p and V_s – a finding that seems to confirm the presence of a magma body in the deep east rift zone. Lastly, Lin et al. (2014a) presented the only V_p/V_s model so far that extends beyond Kīlauea’s summit and rift zones.

3.4 Calculation of noise cross-correlation functions (NCFs)

Noise records for this study were obtained from the permanent short period network on the Island of Hawai‘i (see Figure 3.1 for location) that is operated by the USGS Hawaiian Volcano Observatory (Nakata, 2007; Okubo et al., 2014). The initial dataset includes 2.5 years of continuous data (May 2007 to December 2009), recorded by 38 instruments. During the span of the recordings, most of the short period stations (~80%) were equipped with single-component, vertical-only seismometers, with a natural frequency of 1 Hz. Accordingly, we processed data from the vertical component only in the 0.1-0.9 Hz band, following other ASNT studies that employed fundamental mode Rayleigh waves to image shallow volcanic structures (e.g., Brenguier et al., 2007; Masterlark et al., 2010; Stankiewicz et al., 2010; Nagaoka et al., 2012; Spica et al., 2015; Tamura & Okada, 2016).

Noise cross-correlation functions (NCFs) were calculated after a series of data processing steps. After correcting ~5% of the data for corruption (see Appendix A), we synchronized recording times and processed 12-hour-long single station data series in a similar way as suggested by Bensen et al. (2007): demeaning, bandpass filtering at 0.05-0.95 Hz, decimation from 100 to 10 samples per second, temporal normalization using a running rms value (Masterlark et al., 2010), and spectral whitening. From the processed records, 6-hr-long traces were then cross-correlated (±250 s lag time) for all possible station pairs resulting in two-sided NCFs (i.e., including negative and positive lag times). We normalized these NCFs by multiplying with $1/\sqrt{\sum b_n^2 * \sum d_n^2}$ (b_n and d_n being the data points of the two data series used in the cross-correlation), and then stacked four of them to obtain a daily NCF for each of the 703 station pairs.

3.5 Convergence to Green's functions

As a basic means to ensure data quality for noise-based tomographic imaging, any obvious deviations from the NCFs converging towards the Green's function should be removed from the dataset. We reported such deviations in our prior work (Ballmer et al., 2013; see chapter 2; based on the same dataset and processing as used in this study): both, volcanic tremor and a signal at the NCFs' zero time lag, strongly contaminate the NCFs in certain time windows and frequency bands. We aim at removing contamination by cutting out affected time windows rather than affected frequencies, so as not to compromise depth resolution for ASNT. Although we roughly outlined such time windows already in our prior work, we here examine NCFs in greater detail (i.e., on a daily basis) so that we remove only as many days as necessary from the dataset.

Two station pairs that are located close to the tremor sources (Halema'uma'u and Pu'u'O'o; Figure 3.1) were chosen to identify contaminated days. First, these station pairs are most sensitive to tremor occurrence, as they should exhibit higher tremor amplitudes than station pairs farther away. Second, these station pairs also allow the identification of days that are affected by the signal at the NCFs' zero time lag, because it occurs simultaneously for all station pairs (see section 2.3). When one of the two examined station pairs showed signs of contamination for a given day, we excluded that day's NCFs for all station pairs in our dataset.

Expecting NCFs amplitudes to be relatively high when unwanted signals are superimposed, we used the level of absolute amplitudes in daily NCFs as a quantitative criterion to detect such signals. From our prior work we know that tremor contamination affects NCFs at various time lags in the range of 0.3-0.9 Hz. We therefore addressed tremor contamination by summing absolute amplitudes over the entire length of one daily NCF at 0.3-0.9 Hz and plotted one value for each day for comparison (Figure 3.2, left hand side). Similarly, we know that the puzzling

signal at the NCFs zero time lag occurs at 0.1-0.3 Hz, and hence, we aimed at revealing the days containing this signal by summing absolute amplitudes over two seconds centered on the NCFs zero time lag at 0.1-0.3 Hz (one value for each day is plotted in Figure 3.2, right-hand side). As expected, days with anomalously high amplitudes correspond well to the contaminated time windows outlined in our prior work (see Figure 2.4 in chapter 2). We visually examined the amplitude levels of the four panels in Figure 3.2 and defined a separate threshold for each panel, up to which we consider NCFs to be free of contamination. Only days that pass this criterion for all four panels (i.e., for both station pairs in both frequency bands) were included in the final dataset: about 100 days out of 2.5 years (exact number of days differs between station pairs due to station-specific data gaps).

We then stacked the NCFs of the uncontaminated days into a final NCF for each station pair and checked if the deduced surface wave travel times are generally reasonable. For this purpose, the two sided NCFs of all 703 station pairs were plotted against their inter-station distance (Figure 3.3). Arrival times are clearly observed at increasing lag-times with increasing station separation and are within reasonable bounds for Rayleigh wave group velocities at these frequencies. In the lowest frequency band (i.e., 0.1-0.3 Hz; Figure 3.3a) these arrivals are most distinct, while they get more complex toward higher frequencies (Figures 3.3 b, c and d at 0.3-0.5 Hz, 0.5-0.7 Hz, and 0.7-0.9 Hz, respectively). Accordingly, we are confident that the dataset - although temporally truncated - is generally suitable for surface wave dispersion measurements and subsequent ASNT for Hawai‘i Island. Nonetheless, further quality control is applied during dispersion measurements (section 3.6) and during the inversion (section 3.7). As a final step to further enhance NCF quality, we folded the NCF’s positive and negative side to form the symmetric component (e.g., Bensen et al., 2007).

3.6 Rayleigh wave group velocity dispersion measurements

In order to build a travel time dataset for seismic tomography, we measured Rayleigh wave group velocities with automatic frequency time analysis (FTAN) (e.g., Levshin et al., 1992; Levshin and Ritzwoller, 2001). A narrow Gaussian filter centered on the frequency of interest (0.1-0.9 Hz in steps of 0.01Hz) was applied to each station pair’s final NCF. The envelope of this narrowband signal for each frequency was extracted and plotted as a function of seismic velocity as given by the the inter-station distance divided by the NCF’s lag time (Figure 3.4a shows an example for one station pair). The highest amplitudes of each envelope are assumed to represent the fundamental mode Rayleigh wave with the location of the envelope’s maximum indicating the group arrival time (e.g., Bensen et al., 2007). In a first step, we automatically picked these maxima within a window given by a minimum and maximum acceptable velocity of 0.5 and 4 km/s, respectively. Resulting preliminary dispersion curves for all station pairs are shown in Figure 3.4b.

Because many of the preliminary curves (Figure 3.4b) do not exhibit a naturally smooth shape, we visually inspected each station pair's dispersion curve individually and rejected low quality measurements. The signal to noise ratio (SNR) of a measurement has commonly been applied in previous ASNT studies as a measure for quality. However, it is likely to be unsuitable for the present dataset due to the possibility of remaining volcanic tremor (or of other continuous localized sources) appearing close to the expected Rayleigh wave arrival in the NCFs. Therefore, we disregarded SNR and evaluate a measurement's quality based on its agreement with other measurements. In more detail, we rejected automatic measurements that cause jumps in the dispersion curve (e.g., black parts of the automatically determined dispersion curve in Figure 3.4a) or that are ambiguous due to the presence of other high amplitude signals in the arrival window. Additionally, we rejected measurements at frequencies corresponding to wavelengths greater than one inter-station distance (as applied by Brenguier et al. (2007) and Masterlark et al. (2010)). The resulting selection of dispersion curves (Figure 3.4c) and the total number of remaining measurements at each frequency (Figure 3.4d) reveal a gradual decrease of acceptable measurements toward higher frequencies (maximum of ~460 measurements around 0.18 Hz; minimum of ~120 measurements at 0.9 Hz) – a trend that is likely caused by the decrease of secondary microseismic energy away from it's peak around 0.2 Hz (e.g., Webb et al., 1998).

3.7 2-D inversion procedure

Assuming ray theory acceptable along with straight propagation paths (i.e., along great circles), we set up a linearized inversion problem to obtain group velocity maps at each frequency band. The data consists of the measured group velocity travel times of Rayleigh waves passing between stations; and the yet unknown wave speed model has been parameterized with nodes on a 2x2 km square grid not taking into account topography (an acceptable approximation according to Köhler et al. (2012)). The matrix of partial derivatives that relate changes in the data (the travel times) to perturbations in the slowness model (the reciprocal of the wave speed) essentially contains weighting factors for each model parameter as to how much it effects each propagation path (similar to Dunn et al., 2005) – something that we base on a frequency-dependent zone of influence for each propagation path. Since it is likely that not all model parameters are well resolved by the data, we stabilized the solution by extending the matrix with additional constraint equations in form of damping and smoothing, i.e., penalties on both the magnitude and curvature of the solution. The slowness model can then be determined by finding perturbations to an initially homogeneous starting model (we use the reciprocal of the median of all station pairs' measured group velocities): Travel time residuals (the difference between the measured travel times and those based on the initial model) are calculated and then multiplied by the generalized inverse of the matrix containing the partials. The obtained slowness perturbations are then added to the initial model, with the reciprocal yielding the group velocity map. After choosing an

appropriate smoothing factor with regard to the ability of recovering sharp velocity contrasts of checkerboard resolution tests with 15x15 km velocity heterogeneities, the damping parameter is determined through the L-curve criterion, i.e., considering the trade-off between rms misfit and model variance (such as in Lin et al. (2014a) for example).

The final group velocity maps, however, were not obtained through one inversion for each frequency, but with a bootstrap approach to the above described method followed by additional data revisions. In order to highlight the effect of remaining bad measurements, we set the initial damping parameter intentionally low. With this setting, we performed 1000 separate inversions, each with 90% of the data, selected randomly. The results were averaged into a preliminary group velocity map and the standard deviation (std) was calculated (Figures 3.5a and b show 0.16 Hz as an example). As suspected for an under-damped inversion with data inconsistencies, the resulting group velocity maps show artifacts (e.g., group velocity as high as 8 km/s at the western margin of the model for 0.16 Hz, Figure 3.5a). Considering that bad measurements (i.e., inconsistent with the majority of measurements) are likely to alter an under-damped velocity model considerably when included in the inversion versus excluded from the inversion, we identified bad measurements based on how much they contribute to the std map. Hence, we assigned each propagation path a value for its std contribution by calculating the forward problem in the following way:

A·**std**=**std_c**, with **A** being the same matrix of partial derivatives as used for the inversion, **std** being a vector of standard deviations from the bootstrap approach, and **std_c** being a vector with each propagation path's contribution to the std. Each **std_c** value was then divided by the respective propagation path length providing std contribution per unit length.

The number of propagation paths with a certain std contribution is shown in Figure 3.5c. At low frequencies (0.12-0.22Hz) a majority of propagation paths occupies a very narrow range at low std contribution suggesting that measurements are consistent. At higher frequencies, however, std contributions of propagation paths are much more spread out and tend to be generally higher, meaning that the velocity measurements do not agree as well with each other as at low frequencies – a trend that is very similar to the decrease in number of hand-selected dispersion measurements toward higher frequencies (see section 3.6).

In order to find an appropriate cutoff value for the exclusion of propagation paths with high std contribution, we investigated the effect on the model of different cutoff values for each frequency. As the main criterion, we use the occurrence of unrealistically high velocities in the model. For this purpose, we performed inversions for all possible cutoff values, where propagation paths with higher std contribution are excluded. At each frequency we then plotted the model's highest group velocity for each cutoff value (Figure 3.5d). A distinct jump from reasonable to unreasonable values for most frequencies allowed for a straight-forward selection

of the cutoff value, i.e., so that the model would include a maximum of propagation paths while avoiding unrealistic velocity extremes (we chose the cutoff value so that the model's maximum velocity would not deviate more than 250% from the median velocity). With the resulting refined dataset we determined an appropriate damping factor via the L-curve criterion for each frequency and performed one final inversion that lead to the group velocity maps as presented in section 3.8. The number of propagation paths per frequency as used for the inversions is shown in Figure 3.4d, and the location of used and discarded propagation paths for a subset of frequencies is shown in the left-hand panels of Figures 3.6-3.9. We note that the number of propagation paths has considerably decreased in the range 0.24 to 0.36 Hz and also to some extent at 0.64 to 0.78 Hz (Figure 3.4d) due to the occurrence of strong model artifacts for certain datasets (see Figure 3.5d).

3.8 Rayleigh wave group velocity maps

With the refined dataset, we have solved for Rayleigh wave group velocity maps along with checkerboard resolution tests for the considered frequency range (0.1 to 0.9 Hz in steps of 0.02 Hz). Comparing the resulting images, we found that velocity structures vary mostly smoothly from frequency to frequency as expected based on successively changing surface wave penetration depths. In Figures 3.6-3.9 inversion results along with map plots of the underlying velocity measurements are presented at just eight frequencies. These were selected so that characteristic features of the underlying data and of the resulting models are well represented across the total frequency range, resulting in more images at lower frequencies where sampling differences are larger. Plots of group velocity maps at all frequencies are shown in Figures B.1 and B.2 in the Appendix.

The low-frequency models (0.12, 0.16 and 0.2 Hz; Figure 3.6 and top panels of Figure 3.7) are based on the largest datasets (with a maximum at 0.18 Hz, see Figure 3.4d) and cover an extensive area of the island. Good resolution (as tested with a checkerboard test with 15x15 km velocity heterogeneities) is achieved across most of the southern part of the island including Kīlauea and Mauna Loa with their summits and rift zones and, for 0.16 and 0.2 Hz, as far north as Mauna Kea (see right-hand panels in Figures 3.6 and 3.7). Most of these geologic structures are well delineated by the imaged heterogeneities except for Mauna Loa's northeast rift zone that does not show any obvious correlation with structures in the seismic images. High velocities (relative to the average for each image) appear beneath Kīlauea's rift zones and summit, and Mauna Loa's southwest rift zone and summit (but not at 0.12 Hz, where the summit does not show any anomalies; compare Figure 3.6b with Figures 3.6e and 3.7b). Low velocities dominate between these areas, particularly south of the Hilina fault zone, north of Kīlauea's east rift zone, in-between the summits of Kīlauea and Mauna Loa, and west and northwest of Mauna Loa's

summit all the way to Hualālai (Figures 3.6b, 3.6e and 3.7b). A moderately high velocity feature is imaged just north of Mauna Loa's summit at 0.16 Hz replaced by a strong low-velocity anomaly at 0.2 Hz (compare Figure 3.6e with 3.7b). Considering the underlying data (Figures 3.6d and 3.7a) it seems that the fast anomaly is mainly based on the appearance of one measurement, thus not a robust feature of the image. Moreover, the high-velocity feature that characterizes Mauna Loa's southwest rift zone is confined to the lower rift zone at 0.12 Hz, whereas it extends toward the summit and into the southeast flank at 0.16 Hz and 0.2Hz (compare Figures 3.6b, 3.6e, and 3.7b). Besides these dominant structures, a moderate small-scale velocity contrast of a low-velocity anomaly below the eastern part of Kīlauea's caldera / upper east rift zone area with a high-velocity anomaly to the southwest, is noteworthy at 0.2 Hz (and 0.12 Hz, but a little further down the east rift zone; Figure 3.6b), as it becomes very distinct at 0.26 Hz (Figures 3.7b and e). Additional checkerboard tests for velocity heterogeneities of 6x6 km (see Figure B.3 in the Appendix) suggest that the models up to 0.32 Hz have the potential to recover velocity heterogeneities of this small size, albeit only in Kīlauea's summit / upper rift zones. The amplitudes of imaged velocity anomalies are much stronger for fast features. Whereas slow features deviate from the average velocity by only about -30 to -40%, amplitudes of fast feature deviations are twice as high (~65 - 80%).

The mid- frequency models (0.26, 0.36 and 0.46 Hz, bottom panel of Figure 3.7 and all of Figure 3.8) cover a smaller area than the low-frequency models since acceptable dispersion measurements gradually decrease toward higher frequencies (see Figure 3.4). Whereas the model area at 0.46 Hz represents this gradual trend, the models at 0.26 and 0.36 Hz are within the frequency range where we rejected an anomalously high amount of propagation paths (see Figure 3.5c and d) resulting in much smaller model areas. The southern part of the island around Mauna Loa and Kīlauea however, is well resolved (see Figures 3.7f, 3.8c and 3.8f). Comparable to the lowest frequency models, there are high velocities along Mauna Loa's southwest rift zone (except for 0.36 Hz which does not cover this area) extending into its southeast flank, and beneath Kīlauea's east rift and upper southwest rift zone (Figures 3.7e, 3.8b and 3.8e). Also, the low-velocity anomaly in the Hilina fault area is still present in this frequency band, although it is more confined and of lower amplitude compared to the low-frequency models. The velocity structure beneath Kīlauea's and Mauna Loa's summits, however, is different from the rather high values in the lower frequency band: Whereas a sharp contrast of a distinct low-velocity anomaly in Kīlauea's summit / upper east rift zone area (similar in size to Kīlauea's caldera) with a high-velocity anomaly to the southwest at 0.26 Hz (Figure 3.7e) can also be observed at 0.2 Hz (compare Figure 3.7e with 3.7b), Kīlauea's summit is mostly dominated by low velocities at 0.36 and 0.46 Hz (Figures 3.8b and e). Mauna Loa's summit is characterized by rather low velocities throughout this frequency band, although there are small-scale features of moderately high velocity present in the summit area. The bigger-scale features around Kīlauea and Mauna Loa are generally well determined based on the checkerboard resolution tests, whereas smaller-scale features can only be recovered in Kīlauea's summit and upper east rift zone up to ~0.32 Hz, but

not in Mauna Loa's summit area (as tested with 6x6 km checkerboard tests; Figure B.3 in the Appendix). Comparable to the low-frequency images, the amplitudes of low-velocity anomalies deviate by about -35% from the average velocity, whereas the amplitudes of high-velocity features reach one of the highest deviations from the average at 0.26 Hz (143%) and moderate values of ~80% at 0.36 and 0.46 Hz.

The high-frequency models (0.6 and 0.8 Hz, Figure 3.9) cover a considerably smaller area around Mauna Loa and Kīlauea, mainly due to rejected propagation paths in the southwest and northeast of the island (see Figures 3.9a and d), though the area covered by the model at 0.6 Hz is still comparable to mid-frequencies (0.46 Hz). Whereas Kīlauea's summit still shows moderately low velocities at 0.6 Hz, it is dominated by relatively high velocities at 0.8 Hz just as its rift zones at both frequencies. The contrast between the high velocities along Kīlauea's rift zones with low velocities in the Hilina fault system to the south is a robust feature throughout all frequency bands. Similar to mid-frequencies, Mauna Loa's summit shows moderately high velocities surrounded by an extensive low-velocity zone to the west and north at 0.6 Hz, whereas this area is not resolved at 0.8 Hz. Two small-scale low-velocity features that were already present, but less pronounced, at 0.46 Hz become very distinct at 0.6 Hz: one, just southeast of Mauna Loa's caldera, and the second located further toward the northeast, just south of the northeast rift zone, with an elongated shape in east-west direction (Figure 3.9b). At 0.8 Hz these two features are less pronounced. Based on checkerboard resolution tests, the central part of Kīlauea and Mauna Loa's southeast flank are well determined with resolution quickly decreasing beyond these areas. The amplitudes of imaged velocity features are similar to the low-frequency models ranging from -30% to 65% for slow and fast anomalies, respectively.

3.9 Comparison with previous studies and interpretation

Despite the obvious sampling differences between body waves and surface waves and the inherent differences in depth representation, if we apply the simple rule that the peak depth of Rayleigh wave sensitivity is 1/3 that of the wavelength (as used by Yang&Forsyth (2006) and Spica et al. (2014) for example) the Rayleigh wave group velocity maps can be compared to previous body wave models. The regional body wave images reach as shallow as 2-3 km below sea level (e.g., Okubo et al., 1997; Park et al., 2009; Lin et al., 2014a). Accordingly, only low-frequency Rayleigh wave models overlap in depth representation (peak sensitivity is roughly at 7 km below the surface for 0.12 Hz and ~3.5 km below the surface at 0.2 Hz) with variations dependent on topography (i.e., Kīlauea's caldera lies at ~1 km above sea level and Mauna Loa's caldera at ~4 km). In contrast, mid- and high-frequency models are not well represented by previous studies (except for local studies such as Dawson et al. (1999) that focuses on the uppermost kilometers in Kīlauea's summit area).

At low frequencies, the most obvious similarities with previous studies are the high velocities delineating the volcanic cores of Kīlauea and Mauna Loa with low-velocity anomalies in-between. In particular, the robust contrasts between Kīlauea's summit and rift zones (high) with the Hilina fault system to the south and the Kaoiki fault system in-between Mauna Loa and Kīlauea (low) compare very well to structures imaged in the depth layers down to ~8 km of previous S- and P-models – features that have been interpreted as a contrast between high density magmatic cumulates and volcaniclastic sediments (e.g., Okubo et al., 1997; Park et al., 2009; Lin et al., 2014a; Lin et al., 2014b). Moreover, the high Rayleigh wave velocities that extend from Mauna Loa's southwest rift zone into its southeast flank resemble previously imaged P- and S- wave structures in the upper ~6 km, particularly when considering that Rayleigh wave group velocity maps are sensitive to a greater depth range than the body wave images. This feature has been associated with magmatic pathways, and, because in most images it is mainly located underneath the southeast flank and not the southwest rift zone, a possibility of an abandoned rift zone has been suggested (Okubo et al., 1997; Park et al., 2009; Morgan et al., 2010; Lin et al. 2014a, 2014b; Zurek et al., 2015).

In addition, the low-frequency group velocity maps exhibit features comparable to previous studies that are not part of the main structures described above. The area south of Mauna Kea summit in which we find a high-velocity anomaly resembles a feature of the P-wave model of Park et al. (2009) that was imaged at depths ranging from 3 km below sea level (near the summit) to 10 km (further south) and interpreted as an old rift zone that might have been limited southward by the growth of Mauna Loa. We note that this area is not covered by other earthquake-based studies since long recording times are required to gain sufficient data coverage in an area where stations and earthquakes are sparse (Park et al. (2009) collected data over 34 years). Another noteworthy feature is the small-scale low-velocity anomaly in Kīlauea's upper east rift zone at 0.12 Hz. Although the anomaly is weak, it is similar in size and location to the low V_s anomaly at 9 km below sea level in the model of Lin et al. (2014b) that has been interpreted as a magma chamber due to its coincidence with a high V_p/V_s anomaly. Given that the peak sensitivity of 0.12 Hz is a little shallower than 9 km and that the anomaly disappears toward higher frequencies, the model at 0.12 Hz might likely cover the top of the potential magma chamber.

Although mid-frequency models do cover structures beyond Kīlauea summit (where the imaged features look similar to low frequencies), Kīlauea's caldera is the only area comparable to previous studies due to very limited prior results for these shallow depths. The most striking feature of the mid-frequency models is the small-scale low-to-high-velocity contrast below the southern part of Kīlauea's caldera appearing between 0.2 and 0.3 Hz (maximum sensitivity at ~3.5-2 km depth) – a feature remarkably resembling the model of Dawson et al. (1999), where a similar low-to-high contrast in P-wave velocities has been imaged at ~1-2.5 km below sea level (with Kīlauea's caldera being at ~ 1 km above sea level, these depths correspond to ~ 2-3.5 km

below the surface). At shallower depths, the velocity contrast in the model of Dawson et al. (1999) turns into a broader P-wave anomaly centered on the southern rim of the caldera – a change that is also imaged by the group velocity maps presented here, showing low velocities in Kīlauea's caldera at frequencies above 0.3 Hz (at these higher frequencies, however, resolution is not sufficient for small-scale features). Because the P-wave anomaly coincides with a two-fold high V_p/V_s anomaly, the feature has been interpreted as a magma storage zone (Dawson et al., 1999). In addition to this interpretation, parts of the low velocity features in this area might well be caused by hydrothermal effects, the surface and near-surface expressions of which have been documented along the upper east rift zone - particularly in the Puhimau thermal area (Dunn and Hardee, 1985; Bartel and Jacobson, 1988; McGee et al., 2006).

Mauna Loa's elevation at ~ 4 km above sea level sets its shallow structures in the summit area outside the resolved depth levels of previous tomography studies. Nonetheless, the low-velocity anomalies south-southeast of Mauna Loa's caldera imaged at mid-to-high frequencies (i.e., consistently appearing at ~0.22 – 0.9 Hz) possibly represent a magma storage system that has been proposed by numerous studies (based on deformation and tilt) to be located in this area at depths of ~ 3-4 km (overview given by Poland et al., 2014).

In addition to body wave tomography studies, density models based on residual gravity data provide insight into the volcanic structures and can be compared to the Rayleigh wave group velocity maps. Kauahikaua et al. (2000) and Flinders et al. (2013) inverted gravity data and found that high-density bodies outline the cores of the volcanoes, where high-density olivine-rich cumulates and intrusive complexes are indicative of magma pathways. Considering that these high-density bodies span almost the entire depth range down to ~20 km (Flinders et al., 2013), it is not surprising to find good agreement with the location of fast-velocity features imaged in the low-frequency Rayleigh wave models. In particular, the high velocities underneath Kīlauea's summit, east rift zone and upper southwest rift zone, as well as the broad high-velocity zone in Mauna Loa's southwest rift zone / southeast flank match very well with the extension of the gravity-based high-density bodies. Moreover, the location of the high-velocity anomaly south of Mauna Kea's summit correlates with the southward extension of the high-density body centered beneath Mauna Kea in the model by Kauahikaua et al. (2000), although this feature is much more confined to the summit area in the model by Flinders et al. (2013).

In contrast to the high-density bodies, the gravity-based models also reveal areas that stand out for their lack of high-density material. These areas are located north of Kīlauea's east rift zone as well as to the Northwest of Mauna Loa's summit, in-between Hualālai and Mauna Kea (Kauahikaua et al., 2000), which coincide with the location of noticeable low-velocity anomalies in the Rayleigh wave group velocity images. The distance of these areas to the volcanic centers together with the low density of the material suggests that the low velocities here most likely represent physical property effects, such as increased porosity that might be expected for lava

flows or volcaniclastic sediments, as has been interpreted for the Kaoiki and Hilina Fault zone areas described above.

3.10 Discussion and Conclusion

Although the obtained Rayleigh wave group velocity maps agree very well with previous results, the removal of volcanic tremor from the daily NCFs and the resulting temporally truncated dataset raise the question whether the used dispersion measurements and thus the obtained velocity maps might be biased. Ocean-generated noise sources are typically directive and thus they generally do not meet the theoretical requirement of a homogeneous noise source distribution (e.g., Yang & Ritzwoller 2008). This condition suggests a requirement for NCFs to be stacked over at least a year, so that the seasonally-varying noise field be averaged and yield a more uniform distribution. Meanwhile, numerous studies have investigated the effect of non-homogeneously distributed sources and developed corrective methods for the induced bias (e.g., Tsai, 2009; Weaver et al., 2009; Yao & van der Hilst, 2009; Froment et al., 2010; Harmon et al., 2010). However, these studies have shown that biases of recovered velocity structures tend to be small (<1%) (e.g., Froment et al., 2010; Harmon et al., 2010) even for short recording times (e.g., one month-long as demonstrated by Yao and van der Hilst, 2009, for data from Tibet). Noise-source-distribution-induced biases therefore seem to be negligible even for the short stacking time (i.e., three months) in this study. It remains to be investigated, however, whether the location of Hawai‘i in the middle of the Pacific ocean results in a more homogeneous noise source distribution than in continental setting, or whether the strong seasonal variability in dominant ocean wave direction (e.g., Willis et al., 2004; Yang & Ritzwoller, 2008) has an adverse effect in this setting.

Even if biases from a non-homogeneous source distribution were negligible, superimposed signals from persistent localized sources can strongly affect the ability of retrieving accurate dispersion measurements from NCFs. Whereas our dataset showed obvious signs of contamination of one such source (i.e., volcanic tremor in addition to possibly electric noise) that we removed, we cannot rule out precursory arrivals in the NCFs caused by the presence of less obvious signals such as remaining volcanic tremor, higher modes energy (e.g., Kimman et al., 2012) or arrivals from near-coastal wave action (e.g., Tian & Ritzwoller, 2015). Especially the high number of inconsistent measurements at limited frequency bands (i.e., at 0.24 to 0.36 Hz and also to some extent at 0.64 to 0.78 Hz) might be due to contamination, though the origin remains unknown (we note that these frequency bands are different from those bands where volcanic tremor has been clearly identified (Ballmer et al., 2013; see chapter 2)). In order to avoid such contaminations causing biased velocity models, we rejected a high number of inconsistent measurements. Nonetheless, a noticeable disparity between amplitudes of fast and slow velocity anomalies (particularly pronounced in the above mentioned frequency bands)

indicates that measurements used for the inversion might still be biased toward fast velocities. We tested a more restrictive data rejection (i.e., a lower cutoff values for the std contribution), but found that imaged velocity anomaly patterns remained virtually unchanged, except for a strong decrease of the area resolved by the models.

A more thorough investigation of the local noise characteristics together with possibly longer time series will likely be the most important step towards more complete data coverage and thus higher resolution ASNT models in the future. In the present models, data coverage gradually decreases towards higher frequencies due to data rejections for quality reasons. Another improvement may result from inversion for noise source distribution in addition to velocity structure (e.g., Ermert et al., 2016). Nevertheless, the current velocity models are robust and meaningful within the resolved area, even for only three months of data, as shown by comparison with previous studies (see section 3.9). Temporally truncating the dataset in order to avoid the contamination by volcanic tremor does not seem to have a fundamental impact on ASNT in Hawai‘i. These promising results demonstrate the high potential of ASNT in Hawai‘i to provide independent constraints on S-wave structure, particularly in view of long recording times and/or dense station arrays that are needed for high-resolution earthquake-based tomography. Thereby, we provide a first step towards possible time-dependent three-dimensional seismic tomography (e.g., Julian & Foulger, 2010; Koulakov et al., 2016) based on repeated ambient noise tomography.

3.11 Figures

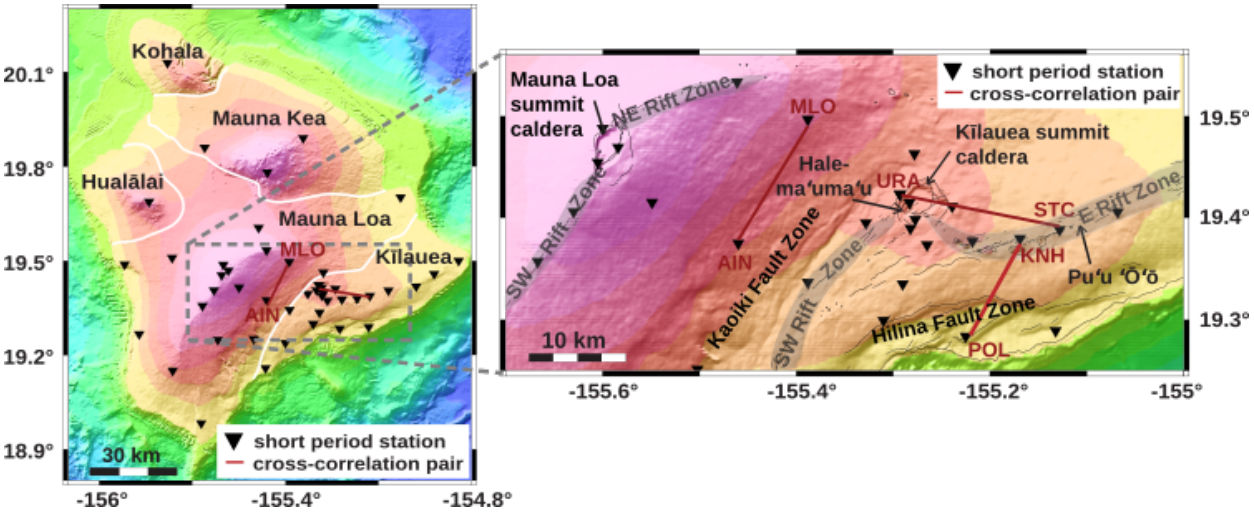

Figure 3.1: Topographic map of the Island of Hawai'i (white lines outline volcano boundaries). Black triangles indicate the locations of stations that make up the USGS HVO short period seismic network. Red lines and three-letter names highlight those station pairs that are later referred to in the text and in Figure 3.2. The inset shows parts of Kīlauea and Mauna Loa including geologic structures such as summit calderas and craters (black arrows), rift zones (grey shading), and faults (grey lines).

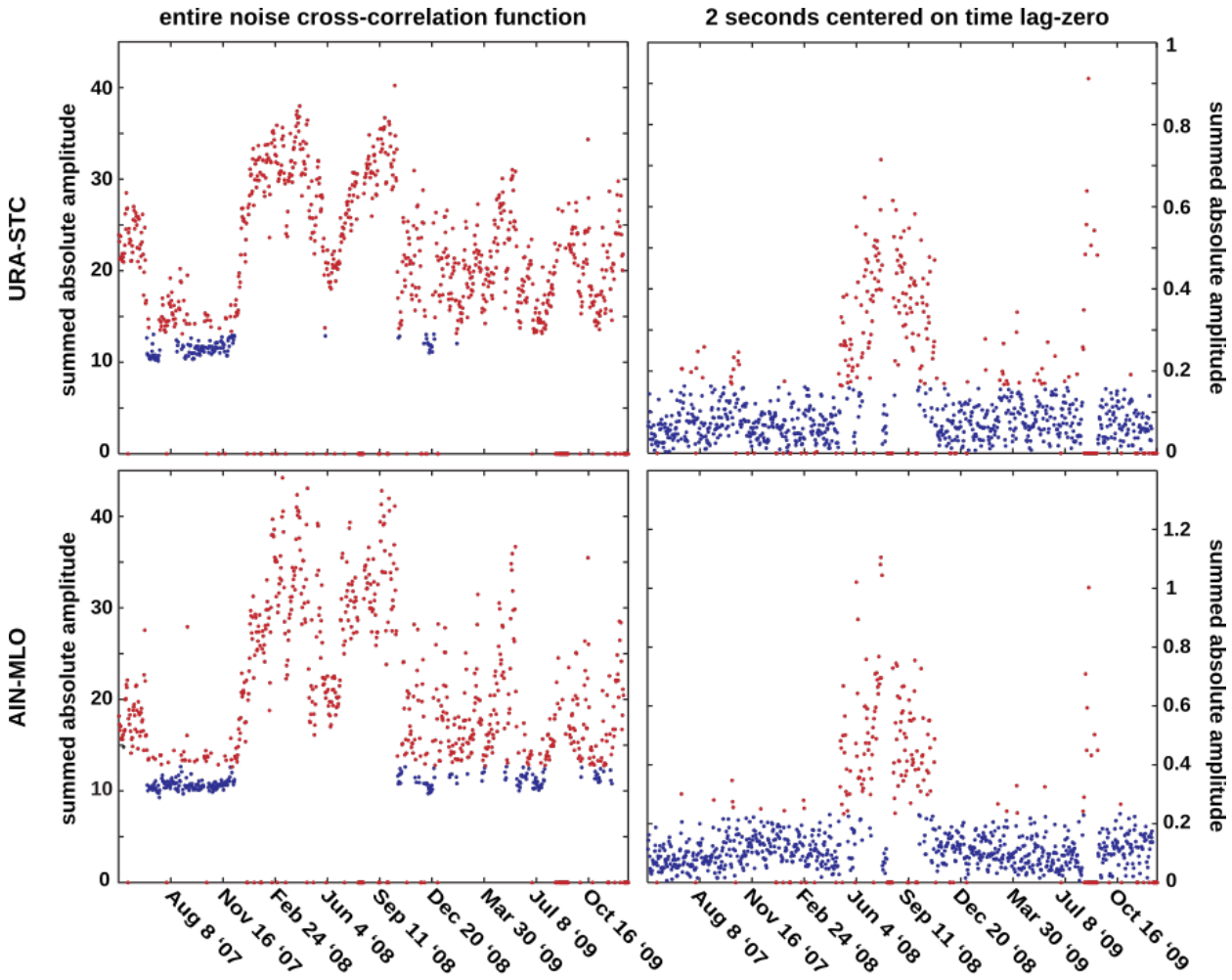

Figure 3.2: Amplitudes of noise cross-correlation functions (NCFs) versus time for two station pairs (top row is pair URA-STC, bottom row is pair AIN-MLO; locations of the pairs are shown in Figure 3.1). Each point represents a daily NCF. Amplitudes shown are absolute amplitudes summed over the entire NCF (left) and over two seconds centered on the time lag of zero (right). Zero amplitudes are data gaps. High amplitude points correspond to either tremor-bearing (left) or noise-contaminated (right) time windows, as described in Ballmer et al. (2013), see chapter 2. Daily NCFs of amplitudes above a certain threshold (red color) are excluded from further analysis. See section 3.5 for details.

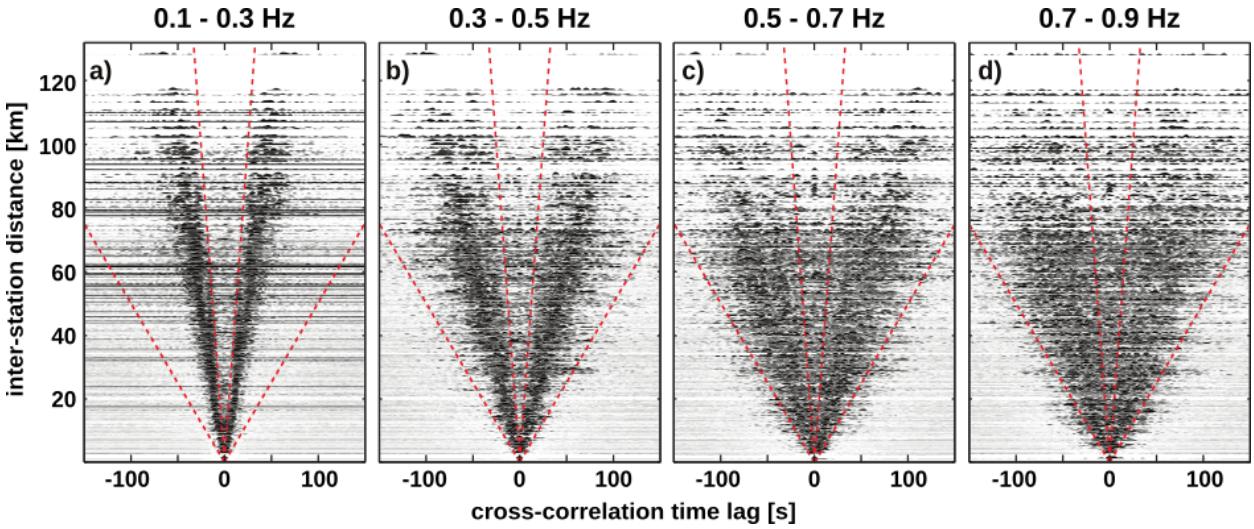

Figure 3.3: Envelopes of two-sided noise cross-correlation functions (NCFs) of all station pairs plotted against inter-station distance in four frequency bands. NCFs are stacked over ~100 uncontaminated days and amplitudes are normalized. Red dashed lines indicate lag times corresponding to group velocities of 0.5 km/s and 4 km/s that will later be used as lower and upper bound, respectively, for acceptable dispersion measurements. Note that moveout patterns are most distinct at 0.1-0.3 Hz and get more complex towards higher frequencies.

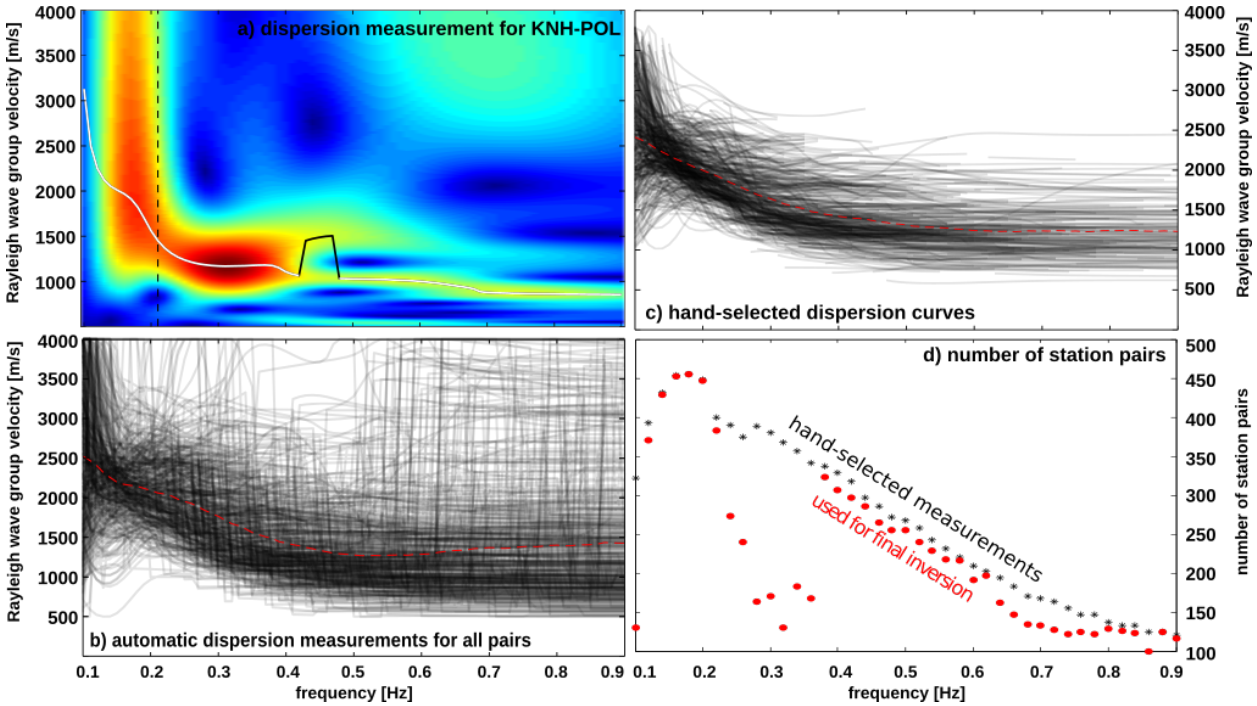

Figure 3.4: Rayleigh wave group velocity dispersion measurements. a) Station pair KNH-POL (see Figure 3.1 for location). Color represents envelope's amplitude (red and blue for high and low amplitudes, respectively) of narrowband filtered NCF at each frequency. Lag times have been mapped into velocity with known inter-station distance. The automatically-picked dispersion curve is shown as solid white/black line. Black parts of this line represent measurements we refused based on visual examination. The vertical black dashed line refers to the frequency at which the wavelength equals the inter-station distance - measurements at lower frequencies are refused too. b) Automatically-picked dispersion curves for all station pairs – i.e., before bad measurements (e.g., black part in (a)) are refused. The red dashed line shows the average. c) Dispersion curves after exclusion of bad automatic measurements as identified by visual examination along with the average (red dashed line). d) Total number of measurements for each frequency (in 0.02 Hz steps) of hand-selected measurements as shown in (c) and as used for final tomographic inversion after further data rejection (see section 3.7).

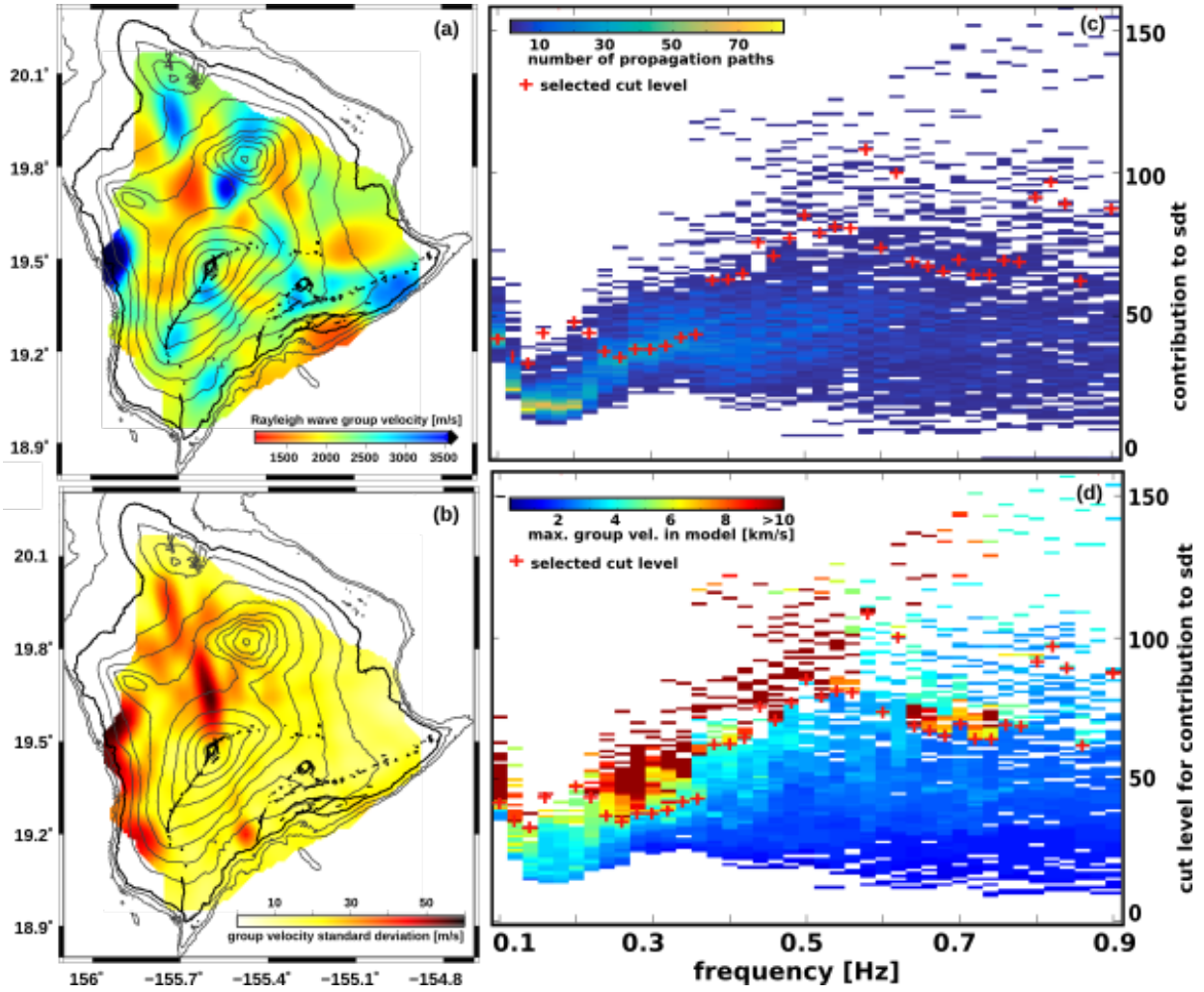

Figure 3.5: Illustration of the data selection criteria during the inversion. a) Rayleigh wave group velocity map at 0.16 Hz obtained from averaging 1000 under-damped trial inversions, each of which uses 90% of the data, selected randomly. Note that the darker blue areas represent values up to ~8 km/s (i.e., exceeding the colorscale's maximum) – an artifact arising from low quality dispersion measurements and being amplified by very low damping. b) Standard deviation of group velocity for the 1000-trial-average. Thick black lines outline the shoreline and geologic features of the Island of Hawai'i; thin black lines show elevation in 500 m intervals. c) Number of propagation paths of a certain contribution to the standard deviation for each frequency. d) Maximum group velocity for models obtained with different cutoff values with regard to the propagation paths' contribution to the standard deviation for each frequency. Note the rather obvious jump to unreasonably high velocities (blue vs. red) for most frequencies. Selected cutoff values for the final inversion are marked by red crosses (i.e., where the model's maximum velocity deviates 250% from the median velocity); propagation paths with higher contribution to the standard deviation are considered low quality.

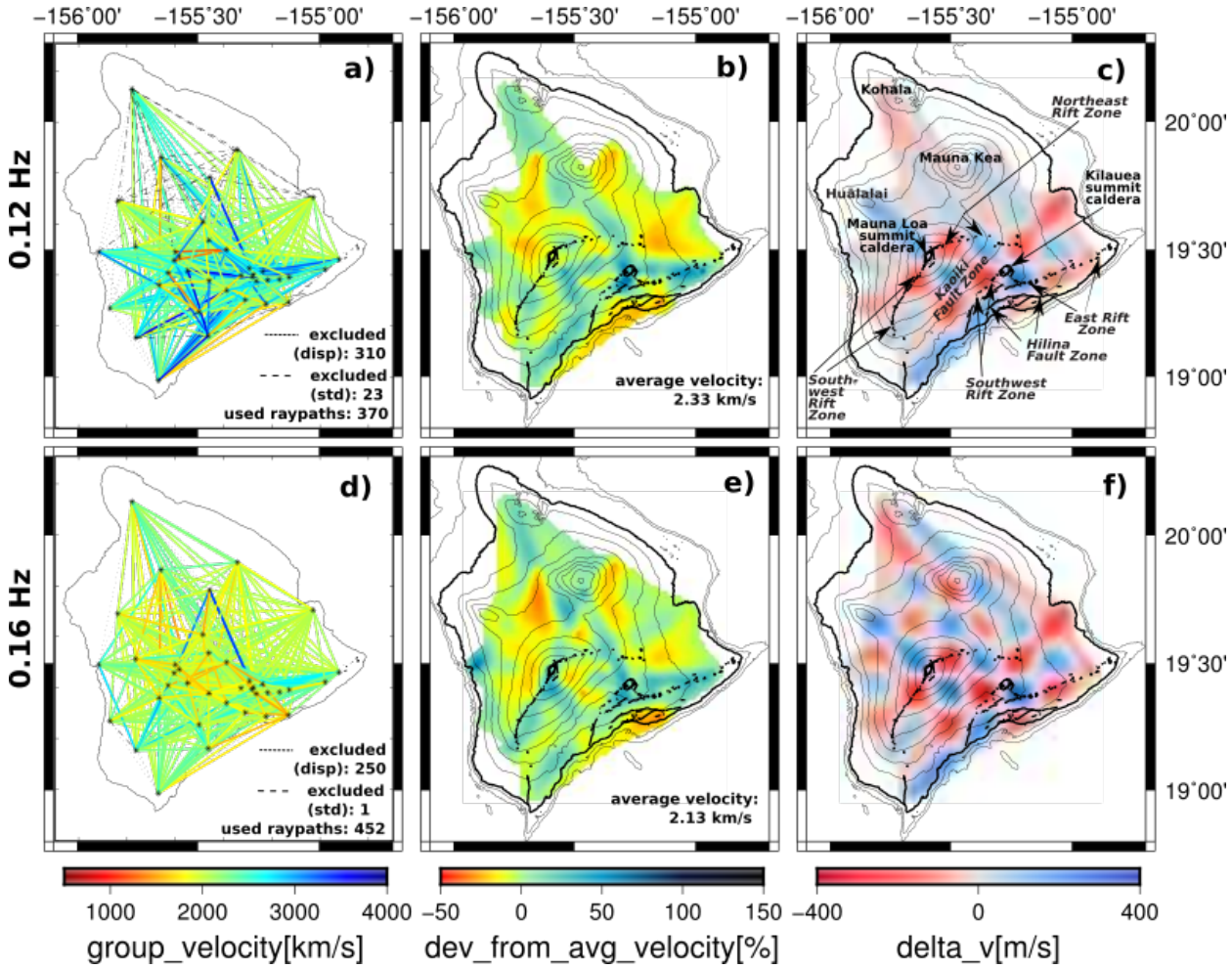

Figure 3.6: Rayleigh wave group velocities on map (a and d) with final models (b and e) and checkerboard resolution tests (c and f) for two frequencies. Panels a and d show in color those propagation paths that were used in the inversion; black dotted and dashed lines indicate locations of paths excluded based on visual examination of dispersion curves and contribution to the model's std, respectively (see text for more details). Checkerboard tests are performed with 15x15 km velocity heterogeneities. Thick black lines in (b,c, e and f) outline the shoreline and geologic features of Hawai'i Island; thin black lines show elevation in 500m intervals. Regions with insignificant ray coverage are masked out (i.e., a derivative weight sum (dws) < 1; see e.g., Toomey and Foulger, 1989 for a definition of dws).

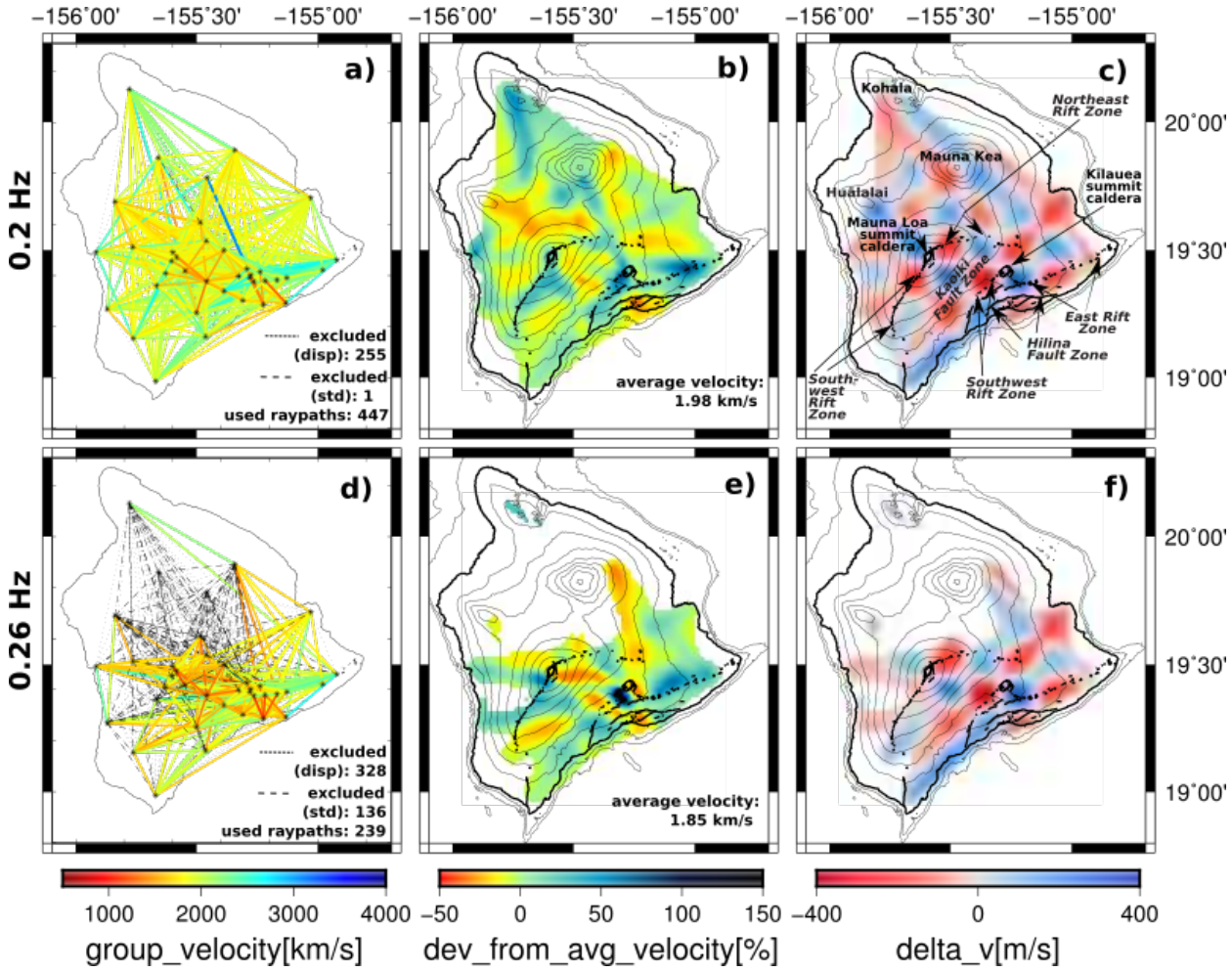

Figure 3.7: Same as Figure 3.6, but for frequencies 0.2 and 0.26 Hz.

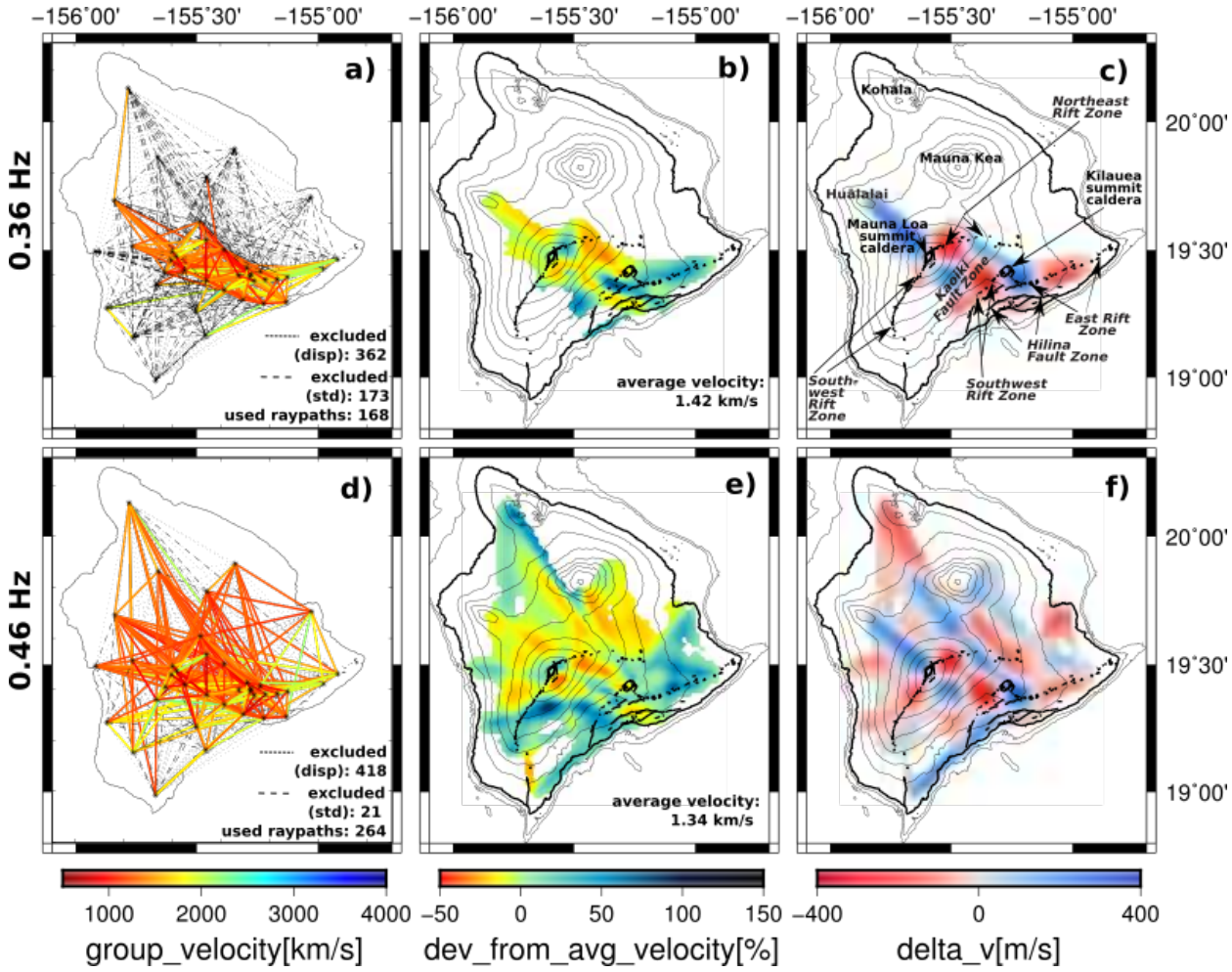

Figure 3.8: Same as Figures 3.6 and 3.7, but for frequencies 0.36 and 0.46 Hz.

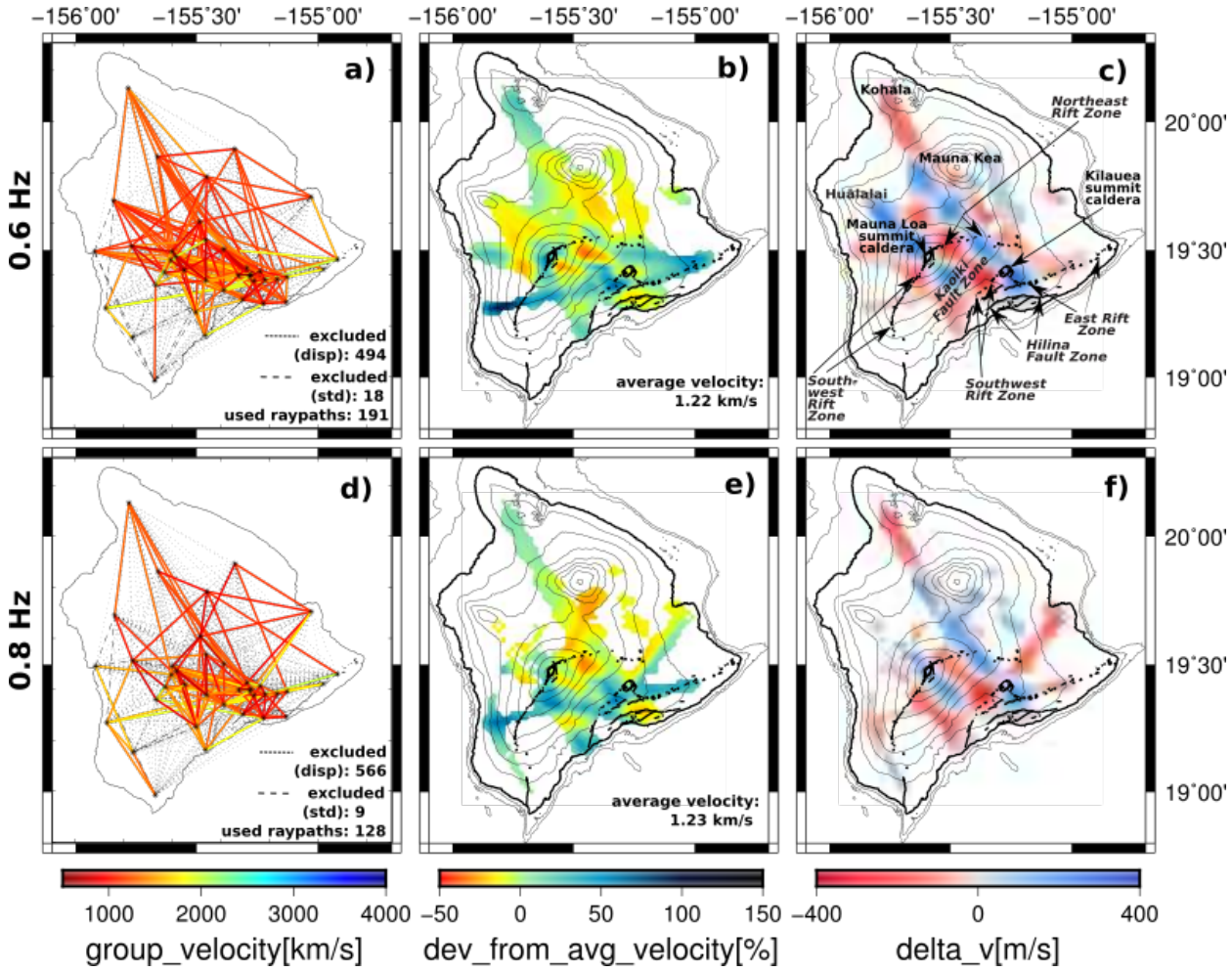

Figure 3.9: Same as Figures 3.6, 3.7 and 3.8, but for frequencies 0.6 and 0.8 Hz.

CHAPTER 4

CONCLUSIONS AND OUTLOOK

With this dissertation, we present the first application of ambient seismic noise interferometry in Hawai‘i. We have shown in chapter 2 that the specific data processing used in this technique does not only extract the coherent part of microseismic noise, but also of volcanic tremor. Remarkably, the tremor signals became observable over large distances (>50km), where they have not been apparent in the raw data. By utilizing these signals for source localization, we have demonstrated how the long-range coherence can help in studying volcanic tremor – an application that is of special interest for volcano monitoring in remote locations, where seismic stations might be far away from the volcano. Building upon the approach presented here a successful application in such a setting has meanwhile been realized, i.e., the characterization of volcanic tremors of a group of volcanoes in Kamchatka (Droznin et al., 2015).

In view of imaging heterogeneity or measuring temporal velocity changes in volcanic regions, however, the results of chapter 2 suggest that ambient seismic noise interferometry might strongly be affected during times of volcanic tremor. Therefore, we have excluded all days that showed signs of tremor contamination in order to perform ambient seismic noise tomography (chapter 3). Although the remaining dataset had been temporally truncated to only three months, we found that the obtained Rayleigh wave group velocity maps are robust and meaningful as verified through comparison with previous seismic studies. Whereas the main volcanic structures had been imaged by a variety of previous body wave studies, some features of the noise-based images could previously only be imaged for special study designs (i.e. regions as far north as Mauna Kea as well as the very shallow subsurface under the summits of Kīlauea and Mauna Loa). However, there is still room for improvement for example through more complete data coverage (obtainable maybe through longer recording times and/or more thorough investigation of the noise cross-correlation functions). Such improved spatial resolution would be the optimal starting point for the calculation of a three dimensional S-wave model.

The effect of volcanic tremor on the ability to measure temporal changes in seismic velocities remains to be investigated. It seems that monitoring subtle changes in the subsurface during times of volcanic activity, i.e., when it is of particular interest to apply this method, is likely to be complicated by volcanic tremor most of the times. Accordingly, one of the next steps could be to find ways around this obstacle. One option would be analyzing frequency bands that are not affected by volcanic tremor only. Whereas restricted frequency content will limit depth sensitivity, another approach could instead focus on station pairs, where the tremor signal in the cross-correlation functions do not interfere with the relevant part of the noise-based Green’s function. Finally, determining the stability of volcanic tremor through time could possibly avoid

limiting spatial sensitivity, because stable signals allow measuring subtle velocity changes even if tremor hampers the noise cross-correlation function from converging to the Green's function (Froment et al., 2010).

Whereas 4D tomography through localization of subtle changes in seismic velocities is still subject of research (Brenguier et al., 2016), time sensitive tomography by repeated tomographic inversions has already been realized using body waves (Julian & Foulger, 2010; Koulakov et al., 2016). According to our results from chapter 3 that were obtained with a temporally strongly restricted dataset, repeated ambient seismic noise tomography for different time periods seems to be feasible. For this application it would be important, however, to investigate temporal variability of the seismic wave field in Hawai‘i: first, in order to determine sensitivity of the results to different seasons, and second, to different length of the dataset – something that could not be achieved with the dataset used here.

APPENDIX A: SUPPORTING INFORMATION ON SEISMIC DATA

The data presented in this study are derived from short-period seismic stations operated by the U.S. Geological Survey's Hawaiian Volcano Observatory (HVO) on the Island of Hawai'i. Analog seismic signals from these stations, until 2011, were transmitted continuously to HVO for analysis and storage. The analog signals were converted into digital time series using Earthworm (Johnson et al., 1995), at a rate of 100 samples/s. Data were archived from a Winston waveserver, written into 12-hour-long SAC waveform files. Although we are unable to track down the cause, errors evidently occurred in saving the data. As a result, waveforms are sporadically corrupted with values of -12345, creating data gaps (see Figure A.1a for an example). This corruption occurs for all stations in the short period network and is most extensive for a 12 month period beginning on November 5, 2007 (Figure A.2). During this year-long period, about 85% of SAC files contain these data gaps, whereas the other ~15% are uncorrupted. The number of bad data points per file is about the same for all stations on a given day, and during most of the year it is at a level of ~200,000 points, i.e., ~1/2 hour per 12-hour-long time series (Figure A.2).

In addition to the data gaps, single point deletions also occur. While a full 12-hour record (including one extra second) consists of 4320100 samples, most of the corrupted data files are shorter due to deletions within the time series. Because both corrupted and uncorrupted files were fortuitously stored for the first 12-hour segment on November 5, 2007 (see Figure A.1 for an example from station URA), we were able to compare both file types and deduce the pattern of deletions. Whereas most data gaps have a length that is a multiple of a full second (i.e., 100 samples or a multiple thereof), some gaps are shortened by one sample (for example 99, 199, or 1299 samples). Comparing the waveforms of corrupted and uncorrupted data, we verified that gaps shortened by one sample contained a single point deletion, introducing timing errors. For all of the corrupted records, we also confirmed that the number of gaps shortened by one sample equaled the number of points that were missing from a full 4320100 sample record. To correct for these single point deletions, we therefore simply insert a data point (set to -12345) whenever one is needed to make a data gap a multiple of a full second. Corrupted files that do not follow this pattern are excluded from further analysis.

In addition, during processing to form noise cross-correlation functions, we set all data gaps to 0 so that they do not contribute to the correlation. However, while this procedure does not seem to affect results in the frequency band 0.1-0.9 Hz, it introduces a very low frequency content (see Figure 2.2 in chapter 2, where spectral amplitudes are high at < 0.05 Hz during the same intervals that bear extensive data corruption as shown in Figure A.2). While at first glance this low frequency content might seem to be associated with the puzzling zero time lag arrival that we occasionally find at 0.1-0.3 Hz (see Figure 2.4 in chapter 2), we note that the interval when the zero time lag arrival occurs does not always correspond to the occurrence of data gaps.

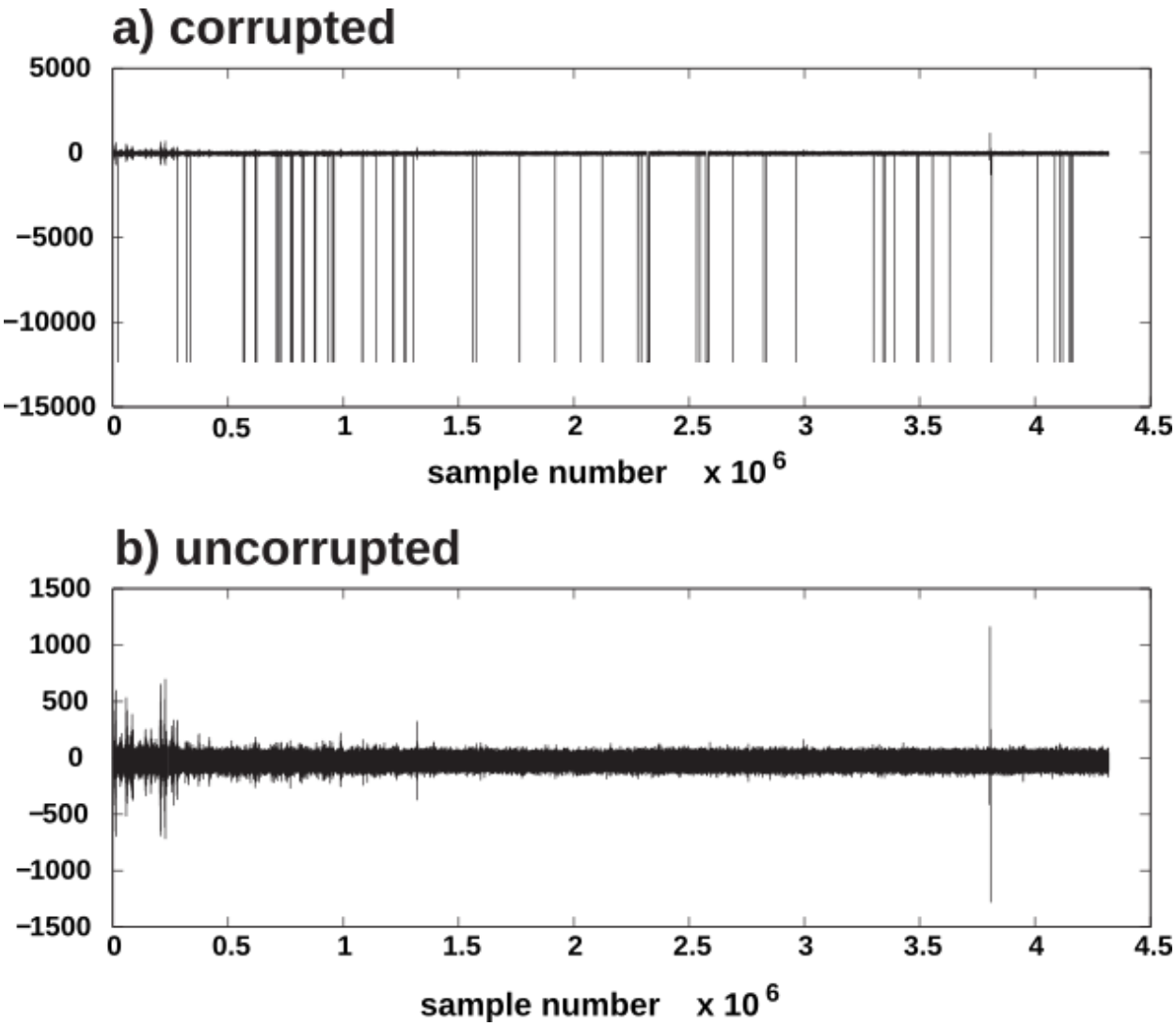

Figure A.1: Corrupted vs. uncorrupted data series for station URA during first 12 hours of 11/5/2007, the only time period where both files types are available. a) Corrupted data series display data gaps that are assigned values of -12345. b) Uncorrupted data series without data gaps.

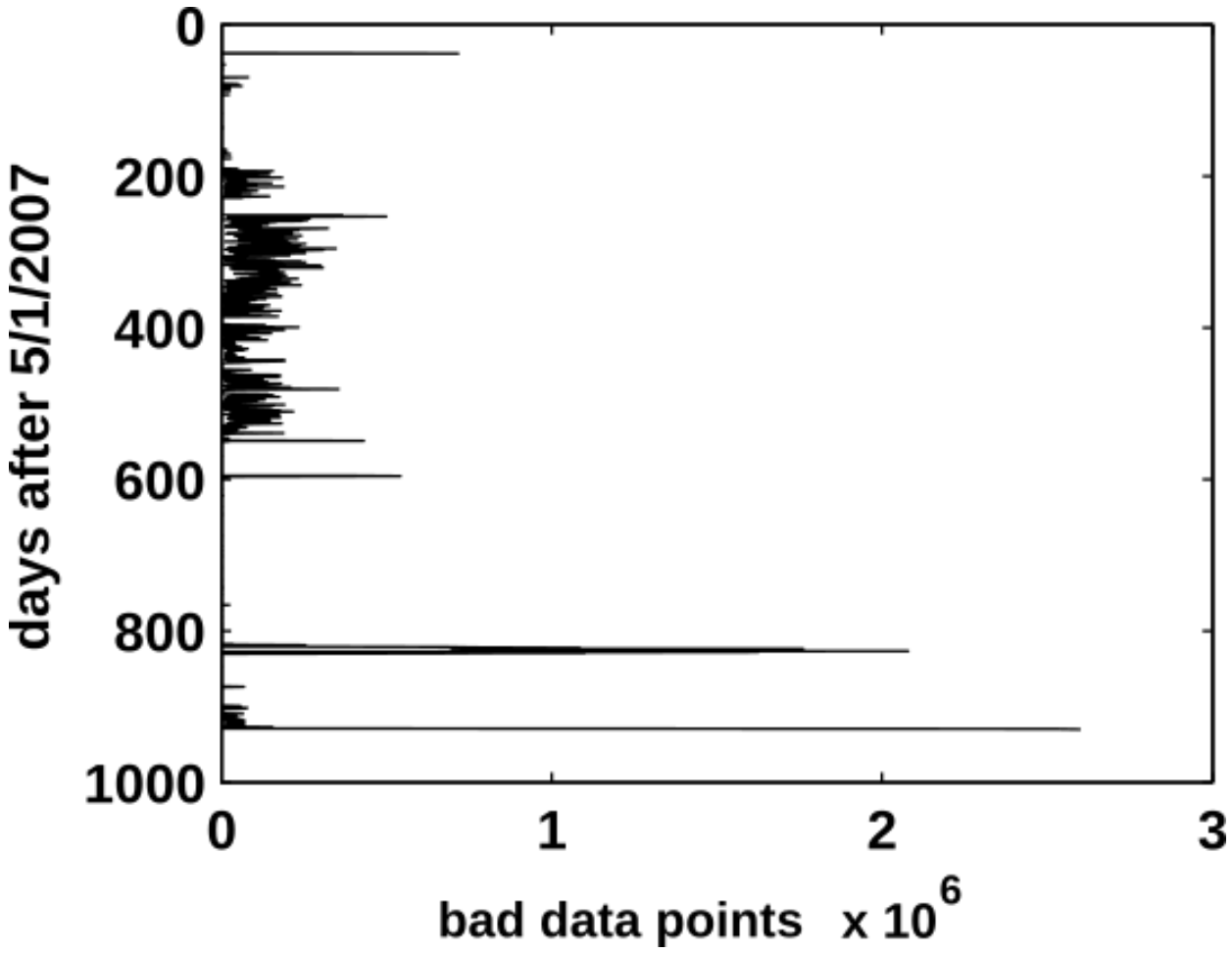

Figure A.2: Number of data gaps (i.e., a value of -12345) for each 12-hour long time series between 5/1/2007 and 12/31/2009 for station URA. Whereas data gaps are present sporadically throughout these 2.5 years, they occur extensively between November 2007 and October 2008.

APPENDIX B: ADDITIONAL TOMOGRAPHIC RESULTS

In addition to the tomographic images for a selection of frequencies (see chapter 3), we here present Rayleigh wave group velocity maps for all frequencies, i.e., 0.12 – 0.9 Hz in steps of 0.02 Hz (Figures B.1 and B.2). In addition, checkerboard resolution tests for 6x6 km velocity heterogeneities are presented for the same frequencies (Figures B.3 and B.4).

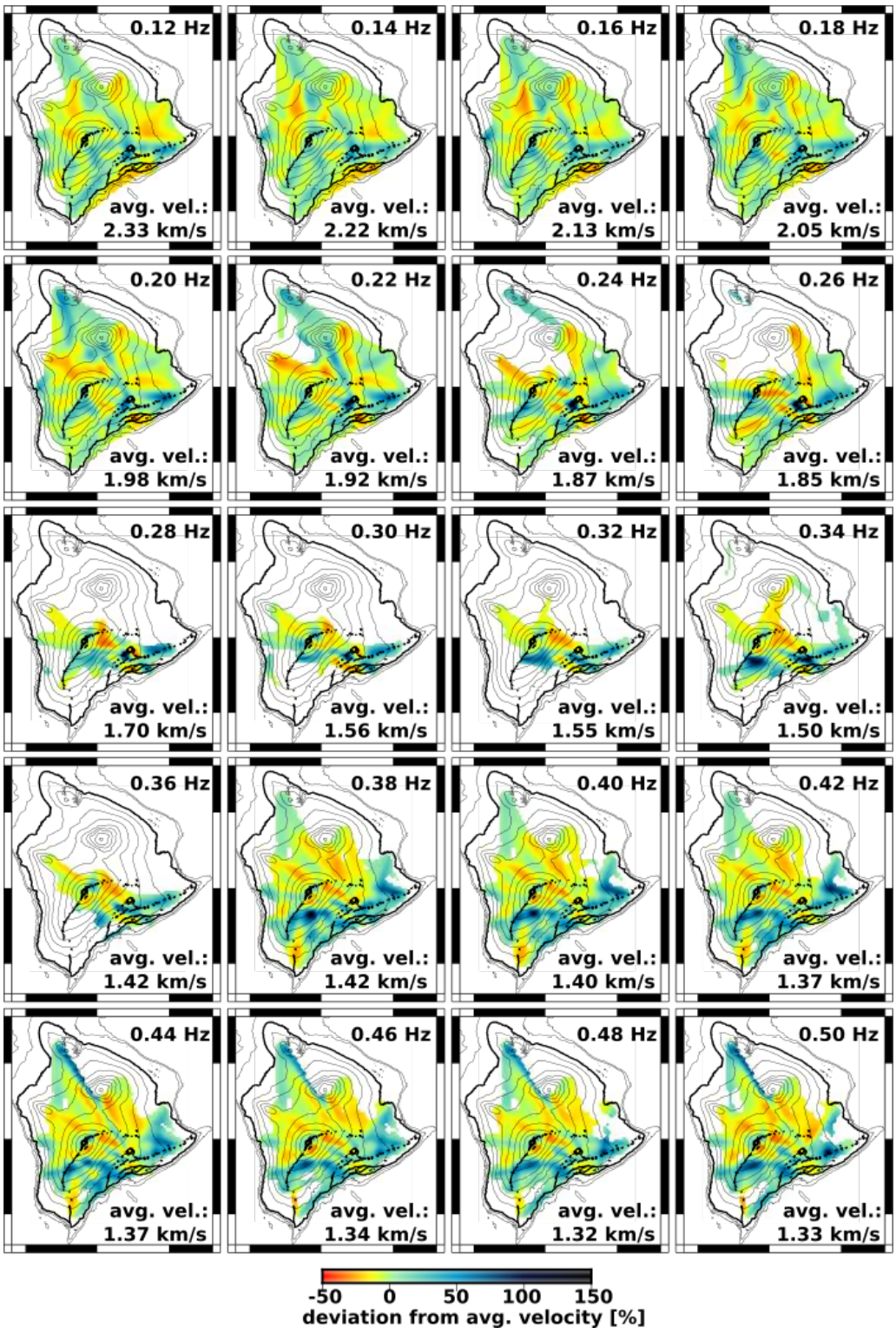

Figure B.1: Rayleigh wave group velocities on maps for 0.12 to 0.5 Hz. Thick black lines in outline the shoreline and geologic features of Hawai‘i Island; thin black lines show elevation in 500m intervals. Regions with insignificant ray coverage are masked out (i.e., a derivative weight sum (dws) < 1; see e.g., Toomey and Foulger, 1989 for a definition of dws).

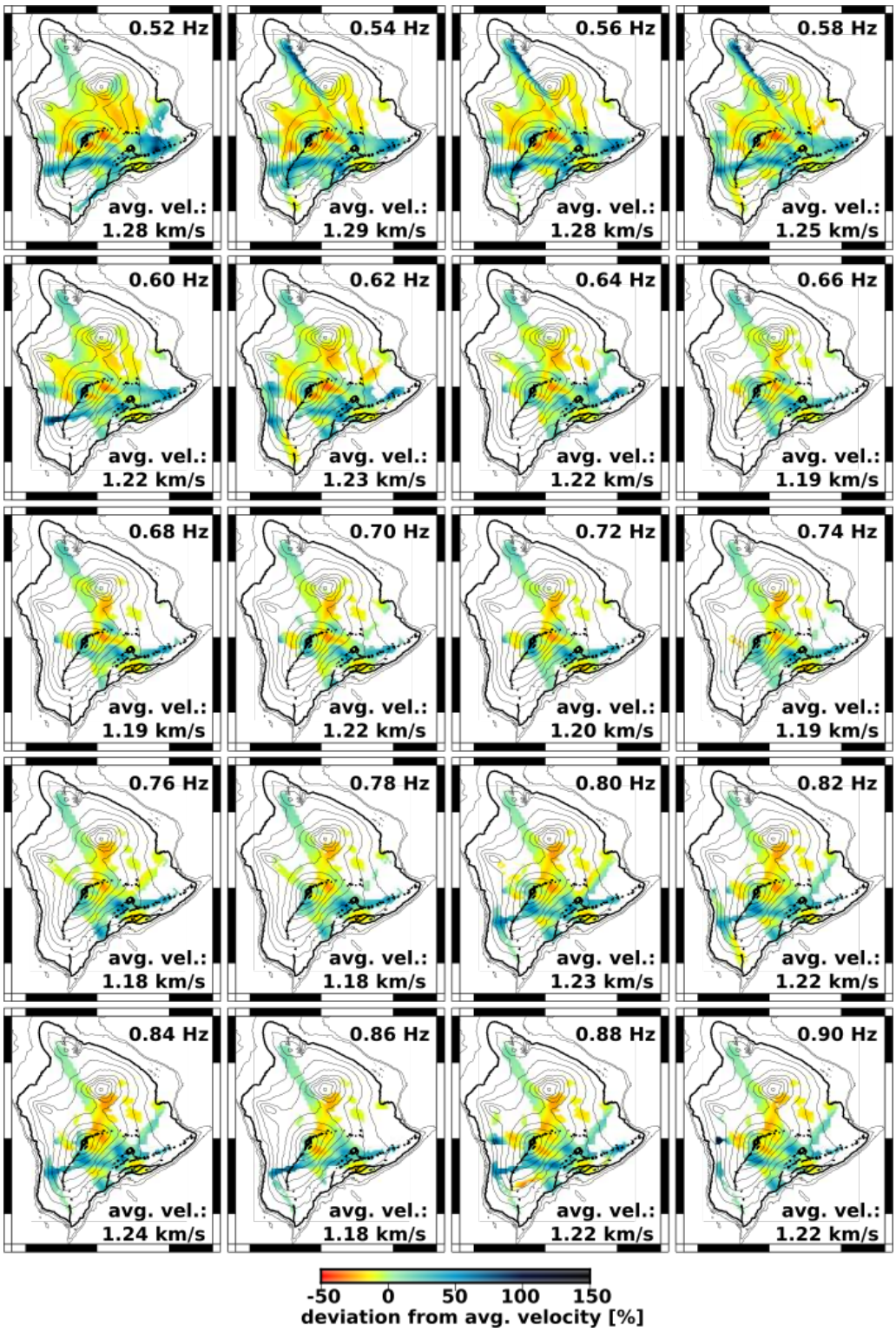

Figure B.2: Same as Figure B.1, but for frequencies 0.52 to 0.9 Hz.

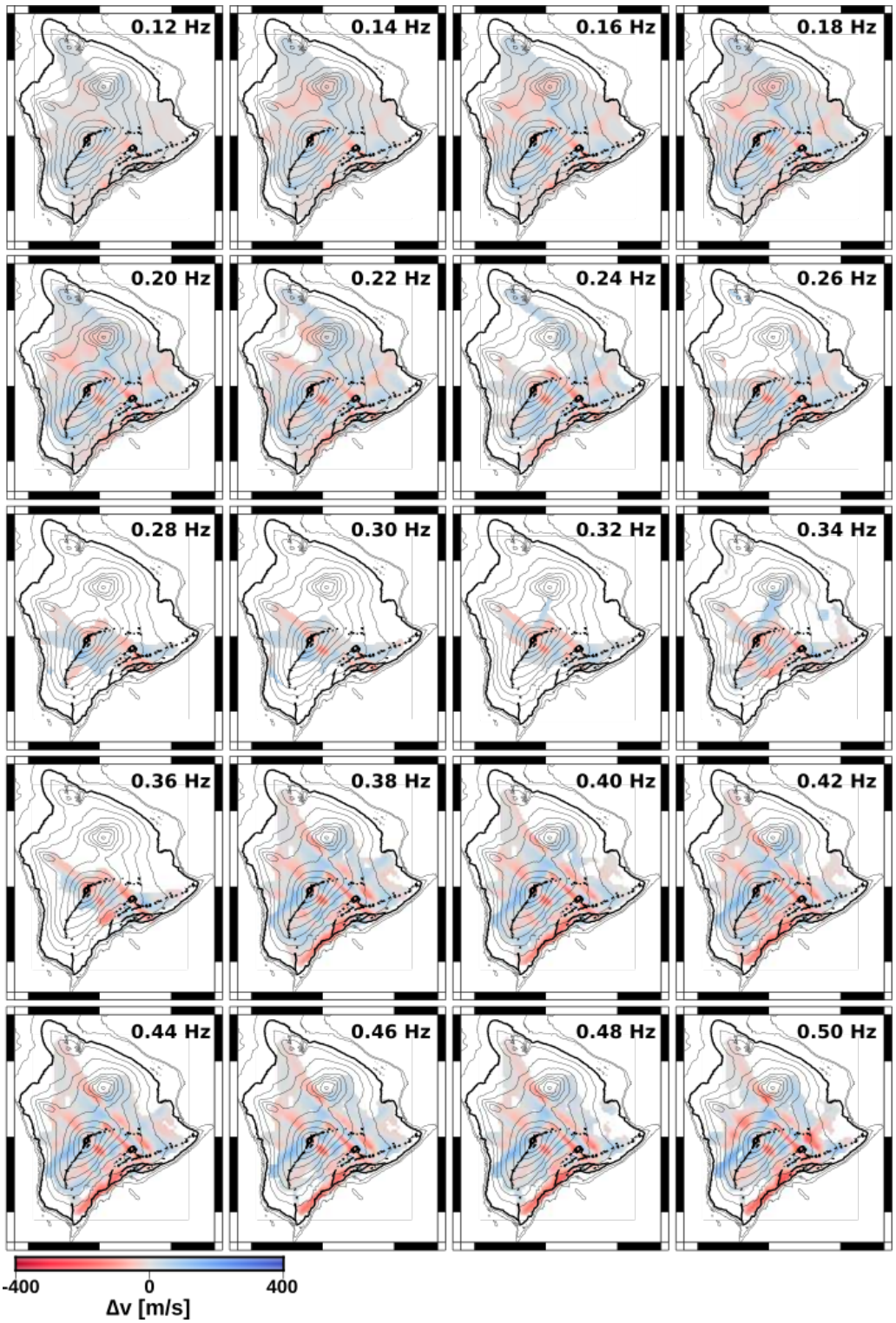

Figure B.3: Checkerboard resolution tests for 6x6 km velocity heterogeneities at 0.12 to 0.5 Hz. Note that small-scale velocity heterogeneities can only be recovered at frequencies up to 0.32 Hz in a small area centered on Kīlauea's upper south flank.

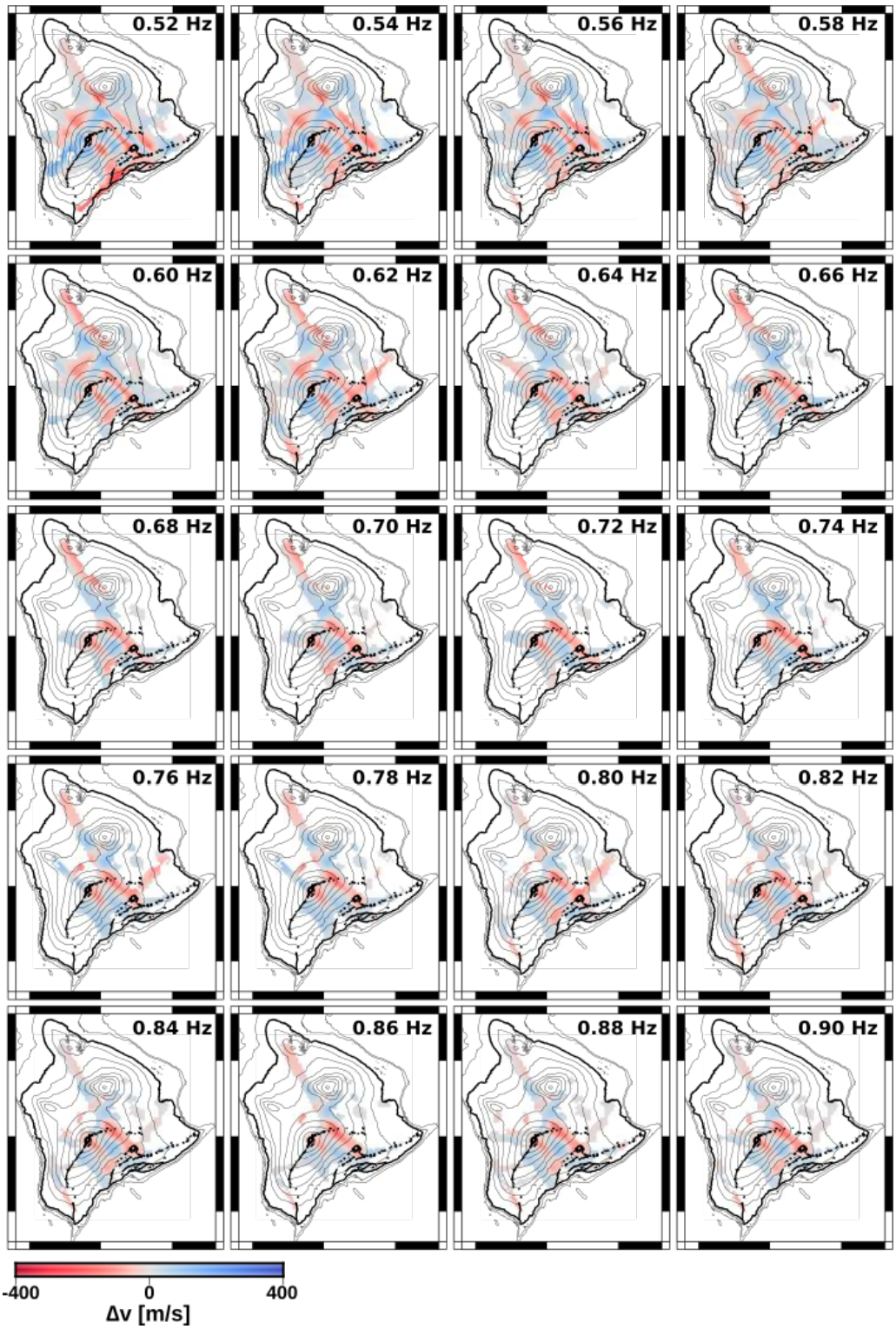

Figure B.4: Same as Figure B.3, but for frequencies 0.52 to 0.9 Hz. Note that small-scale velocity heterogeneities (6x6km) cannot be recovered for these frequencies.

REFERENCES

Almendros, J., J. M. Ibanez, G. Alguacil, E. Del Pezzo & R. Ortiz (1998), Array tracking of the volcanic tremor source at Deception Island, Antarctica, *Geophys. Res. Lett.*, 24(23), 3069-3072, doi:10.1029/97GL03096.

Ballmer, S., C. J. Wolfe, P. G. Okubo, M. M. Haney & C. H. Thurber (2013), Ambient seismic noise interferometry in Hawai‘i reveals long-range observability of volcanic tremor, *Geophys. J. Int.*, *194*, 512-5213, doi:10.1093/gji/ggt112.

Bartel, L. C. & R. D. Jacobson (1987), Results of a controlled-source audiofrequency magnetotelluric survey at the Puhimau thermal area, Kilauea Volcano, Hawaii, *Geophysics*, 52(5), 665–677, doi:10.1190/1.1442334.

Battaglia, J. & K. Aki (2003), Location of seismic events and eruptive fissures on the Piton de la Fournaise volcano using seismic amplitudes, *J. Geophys. Res.*, 108(B8), 2364, doi:10.1029/2002JB002193.

Battaglia, J., K. Aki & V. Ferrazzini (2005), Location of tremor sources and estimation of lava output using tremor source amplitude on the Piton de la Fournaise volcano: 1. Location of tremor sources, *J. Volcanol. Geoth. Res.*, 147, 268-290, doi:10.1016/j.jvolgeores.2005.04.005.

Bensen, G. D., M. H. Ritzwoller, M. P. Barmin, A. L. Levshin, F. Lin, M. P. Moschetti, N. M. Shapiro & Y. Yang (2007), Processing seismic ambient noise data to obtain reliable broad-band surface wave dispersion measurements, *Geophys. J. Int.*, 169(3), 1239-1260, doi:10.1111/j.1365-246X.2007.03374.x.

Brenguier, F., N. M. Shapiro, M. Campillo, A. Nercessian & V. Ferrazzini (2007), 3-D surface wave tomography of the Piton de la Fournaise volcano using seismic noise correlations, *Geophys. Res. Lett.*, 34, L02305, doi:10.1029/2006GL028586.

Brenguier, F., M. Campillo, C. Hadziioannou, N. M. Shapiro, R. M. Nadeau & E. Larose (2008a), Postseismic relaxation along the San Andreas fault at Parkfield from continuous seismological observations. *Science*, 321, 1478-1481, doi:10.1126/science.1160943.

Brenguier, F., N. M. Shapiro, M. Campillo, V. Ferrazzini, Z. Duputel, O. Coutant & A. Nercessian (2008b), Towards forecasting volcanic eruptions using seismic noise, *Nat. Geosci.*, 1, 126-130, doi:10.1038/ngeo104.

Brenguier, F., D. Rivet, A. Obermann, N. Nakata, P. Boué, T. Lecocq, M. Campillo & N. Shapiro (2016), 4-D noise-based seismology at volcanoes: Ongoing efforts and perspectives, *J. Volcanol. Geoth. Res.*, 321, 182–195, doi:10.1016/j.jvolgeores.2016.04.036.

Chouet, B. A. (1996), Long-period volcano seismicity: Its source and use in eruption forecasting, *Nature*, 380(6572), 309-316, doi:10.1038/380309a0.

Chouet, B. A., P. B. Dawson, M. R. James & S. J. Lane (2010), Seismic source mechanism of degassing bursts at Kilauea Volcano, Hawaii: Results from waveform inversion in the 10–50s band, *J. Geophys. Res.*, 115, B09311, doi:10.1029/2009JB006661.

Dawson, P. B., C. Dietel, B. A Chouet, K. Honma, T. Ohminato & P. Okubo (1998), A digitally telemetered broadband seismic network at Kilauea Volcano, Hawaii, *U.S. Geol. Surv. Open-File Report*, 98-108, 122.

Dawson, P. B., B. A. Chouet, P. G. Okubo, A. Villasenor & H. M. Benz (1999), Three-dimensional velocity structure of the Kilauea Caldera, Hawaii, *Geophys. Res. Lett.*, 26, 2805-2808, doi:10.1029/1999GL005379.

Dawson, P. B., M. C. Benitez, B. A. Chouet, D. Wilson & P. G. Okubo (2010), Monitoring very-long-period seismicity at Kilauea Volcano, Hawaii, *Geophys. Res. Lett.*, 37, L18306, doi:10.1029/2010GL044418.

Droznin, D. V., N. M. Shapiro, S. Ya. Droznina, S. L. Senyukov, V. N. Chebrov & E. I. Gordeev (2015), Detecting and locating volcanic tremors on the Klyuchevskoy group of volcanoes (Kamchatka) based on correlations of continuous seismic records, *Geophys. J. Int.*, 203, 1001–1010, doi:10.1093/gji/ggv342.

Dunn, J. C. & H. C. Hardee (1985), Surface heat flow measurements at the Puhimau hot spot, *Geophysics*, 50(7), 1108-1112, doi:10.1190/1.1441983.

Dunn, R. A., V. Lekic, R. S. Detrick & D. R. Toomey (2005), Three-dimensional seismic structure of the Mid-Atlantic Ridge at 35°N: focused melt supply and non-uniform plate spreading, *J. Geophys. Res. 110*, doi:10.1029/2004JB003473.

Duputel, Z., V. Ferrazzini, F. Brenguier, N. Shapiro, M. Campillo & A. Nercessian (2009), Real time monitoring of relative velocity changes using ambient seismic noise at the Piton de la Fournaise volcano (La Réunion) from January 2006 to June 2007, *J. Volcanol. Geotherm. Res*., 184(1-2), 164-173, doi:10.1016/j.jvolgeores.2008.11.024.

Ermert, L., A. Villasenor & A. Fichtner (2016), Cross-correlation imaging of ambient noise sources, *Geophys. J. Int.*, *204*, 347–364, doi:10.1093/gji/ggv460.

Fee, D., M. Garcés, M. Patrick, B. Chouet, P. Dawson & D. Swanson (2010), Infrasonic harmonic tremor and degassing bursts from Halema'uma'u Crater, Kilauea Volcano, Hawaii, *J. Geophys. Res*., 115, B11316, doi:10.1029/2010JB007642.

Froment, B., M. Campillo, P. Roux, P. Gouedard, A. Verdel & R. L. Weaver (2010), Estimation of the effect of nonisotropically distributed energy on the apparent arrival time in correlations, *Geophysics*, 75(5), Sa85-Sa93, doi:10.1190/1.3483102.

Goldstein, P. & B. Chouet (1994), Array measurements and modeling of sources of shallow volcanic tremor at Kilauea volcano, Hawaii, *J. Geophys. Res*., 99(B2), 2637-2652, doi:10.1029/93JB02639.

Got, J.-L., V. Monteiller, J. Monteux, R. Hassani, and R. Okubo (2008), Deformation and rupture of the oceanic crust may control growth of Hawaiian volcanoes, *Nature*, 451, 453–456, doi:10.1038/nature06481.

Groos, J. C., S. Bussat & J. R. R. Ritter (2012), Performance of different processing schemes in seismic noise cross-correlations, *Geophys. J. Int.*, 188(2), 498-512, doi:10.1111/j.1365-246X.2011.05288.x.

Hadziioannou, C., E. Larose, O. Coutant, P. Roux & M. Campillo (2009), Stability of monitoring weak changes in multiply scattering media with ambient noise correlation: Laboratory experiments, *J. Acoust. Soc. Am*., 125(6), 3688–3695, doi:10.1121/1.3125345.

Haney, M. M. (2010), Location and mechanism of very long period tremor during the 2008 eruption of Okmok Volcano from interstation arrival times, *J. Geophys. Res*., 115, B00B05, doi: 10.1029/2010JB007440.

Hansen, S., C. Thurber, M. Mandernach, F. Haslinger & C. Doran (2004), Seismic velocity and attenuation structure of the East Rift Zone and south flank of Kilauea Volcano, Hawaii, *Bull. Seismol. Soc. Am*., 94, 1430–1440, doi:10.1785/012003154.

Harmon, N., C. Rychert & P. Gerstoft (2010), Distribution of noise sources for seismic interferometry, *Geophys. J. Int*., 183(3), 1470-1484, doi:10.1111/j.1365-246X.2010.04802.x.

Harmon, N., T. J. Henstock, M. Srokosz, F. Tilmann, A. Rietbrock & P. Barton (2012), Infragravity wave source regions determined from ambient noise correlation, *Geophys. Res. Lett.*, 39, L04604, doi:10.1029/2011GL050414.

Haslinger, F., C. Thurber, M. Mandernach & P. Okubo (2001), Tomographic image of P-velocity structure beneath Kilauea's East Rift Zone and South Flank: Seismic evidence for a deep magma body, *Geophys. Res. Lett.*, 28, 375–378, doi:10.1029/2000GL012018.

Heliker, C. C., D. A. Swanson & T. J. Takahashi (Eds.) (2003), The Pu'u 'O'o-Kupaianaha Eruption of Kilauea Volcano, Hawaii: The First 20 Years, *U.S. Geol. Surv. Professional Paper* 1676, 206.

Jaxybulatov, K., N. M. Shapiro, I. Koulakov, A. Mordret, M. Landès & C. Sens-Schönfelder (2014), A large magmatic sill complex beneath the Toba caldera, *Science*, 346, 617-619, doi:10.1126/science.1258582.

Jay, J. A., M. E. Pritchard, M. E. West, D. Christensen, M. Haney, E. Minaya, M. Sunagua, S. R. McNutt & M. Zabala (2012), Shallow seismicity, triggered seismicity, and ambient noise tomography at the long-dormant Uturuncu Volcano, Bolivia, *Bull. Volcanol.*, 74(4), 817–837, doi:10.1007/s00445-011-0568-7.

Johnson, C. E., A. Bittenbinder, B. Bogaert, L. Dietz & W. Kohler (1995), Earthworm: A flexible approach to seismic network processing, *IRIS Newsletter*, 14(2), pp. 1-4.

Julian, B. R. & G. R. Foulger (2010), Time-dependent seismic tomography, *Geophys. J. Int.*, 182, 1327–1338, doi:10.1111/j.1365-246X.2010.04668.x.

Kimman, W. P., X. Campman & J. Trampert (2012), Characteristics of Seismic Noise: Fundamental and Higher Mode Energy Observed in the Northeast of the Netherlands, *Bull. Seismol. Soc. Am.*, 102(4), 1388–1399, doi:10.1785/0120110069.

Köhler, A., C. Weidle & V. Maupin (2012), On the effect of topography on surface wave propagation in the ambient noise frequency range, *J. Seismol.*, 16, 221–231, doi:10.1007/s10950-011-9264-5.

Konstantinou, K. I. & V. Schlindwein (2003), Nature, wavefield properties and source mechanism of volcanic tremor: a review, *J. Volcanol. Geotherm. Res.*, 119(1-4), 161-187, doi:10.1016/S0377-0273(02)00311-6.

Koulakov, I., V. Gladkov, S. El Khrepy, N. Al-Arifi & I. H. Fathi (2016), Application of repeated passive source travel time tomography to reveal weak velocity changes related to the 2011 Tohoku-Oki Mw 9.0 earthquake, *J. Geophys. Res. Solid Earth*, 121, 4408–4426, doi:10.1002/2016JB013002.

Lees, J. M. (2007), Seismic tomography of magmatic systems, *J. Volcanol. Geoth. Res.*, 167(1-4), 37-56, doi:10.1016/j.jvolgeores.2007.06.008.

Levshin, A., L. Ratnikova & J. Berger (1992), Peculiarities of surface wave propagation across central Eurasia, *Bull. Seismol. Soc. Am.*, 82(6), 2464-2493.

Levshin, A. L. & M. H. Ritzwoller (2001), Automated detection, extraction, and measurement of regional surface waves, *Pure Appl. Geophys.*, 158, 1531–1545.

Lin, F. C., M. H. Ritzwoller & N. M. Shapiro (2006), Is ambient noise tomography across ocean basins possible?, *Geophys. Res. Lett.*, 33, L14304, doi:10.1029/2006GL026610.

Lin, G., P. M. Shearer, R. S. Matoza, P. G. Okubo & F. Amelung (2014a), Three-dimensional seismic velocity structure of Mauna Loa and Kilauea volcanoes in Hawaii from local seismic tomography, *J. Geophys. Res. Solid Earth*, 119, 4377–4392, doi:10.1002/2013JB010820.

Lin, G., F. Amelung, Y. Lavallee & P. G. Okubo (2014b), Seismic evidence for a crustal magma reservoir beneath the Upper East Rift Zone of Kilauea Volcano, Hawaii, *Geology*, 42, 187–190, doi:10.1130/G35001.1.

Lobkis, O. I. & R. L. Weaver (2001), On the emergence of the Green's function in the correlations of a diffuse field, *J. Acoust. Soc. Am.*, 110 (6), doi:10.1121/1.1417528.

Masterlark, T., M. Haney, H. Dickinson, R. Fournier & C. Searcy (2010), Rheologic and structural controls on the deformation of Okmok volcano, Alaska: FEMs, InSAR, and ambient noise tomography, *J. Geophys. Res.*, 115, B02409, doi:10.1029/2009JB006324.

Matoza, R. S., D. Fee & M. A. Garcés (2010), Infrasonic tremor wavefield of the Pu`u `Ō`ō crater complex and lava tube system, Hawaii, in April 2007, *J. Geophys. Res.*, 115, B12312, doi:10.1029/2009JB007192.

McGee, K. A., A. J. Sutton, T. Elias, M. P. Doukas & T. M. Gerlach (2006), Puhimau thermal area: a window into the upper east rift zone of Kilauea Volcano, Hawaii?, *Pure and Applied Geophysics*, 163(4), 837-851, doi:10.1007/s00024-006-0036-z.

Monteiller, V., J.-L. Got, J. Virieux & P. Okubo (2005), An efficient algorithm for double-difference tomography and location in heterogeneous media, with an application to the Kilauea Volcano, *J. Geophys. Res.*, 110(B12), B12306, doi:10.1029/2004JB003466.

Mordret, A., D. Rivet, M. Landès & N. M. Shapiro (2015), Three-dimensional shear velocity anisotropic model of Piton de la Fournaise Volcano (La Réunion Island) from ambient seismic noise, *J. Geophys. Res. Solid Earth*, 120, 406–427, doi:10.1002/2014JB011654.

Morgan, J. K., J. Park & C. A. Zelt (2010), Rift zone abandonment and reconfiguration in Hawaii: Mauna Loa's Ninole rift zone, *Geology*, 38, 471-474, doi:10.1130/G30626.1.

Nagaoka, Y., K. Nishida, Y. Aodi, M. Takeo & T. Ohminato (2012), Seismic imaging of magma chamber beneath an active volcano, *Earth Planet. Sci. Lett., 333-334*, 1-8.

Nakata, J. S. (2007), Hawaiian Volcano Observatory Seismic Data, January to December 2006, *U.S. Geol. Surv. Open File Report*, 2007-1073, 98.

Neal, C. A., R. G. McGimsey, J. P. Dixon, C. E. Cameron, A. A. Nuzhdaev & M. Chibisova (2011), 2008 Volcanic Activity in Alaska, Kamchatka, and the Kurile Islands: Summary of Events and Response of the Alaska Volcano Observatory, *U.S. Geol. Surv. Scientific Investigations Report*, 2010–5243, 106.

Nishida, K., H. Kawakatsu, Y. Fukao & K. Obara (2008), Background Love and Rayleigh waves simultaneously generated at the Pacific Ocean floors, *Geophys. Res. Lett.*, 35, L16307, doi:10.1029/2008GL034753.

Okubo, P. G., H. M. Benz & B. A. Chouet (1997), Imaging the crustal magma sources beneath Mauna Loa and Kilauea volcanoes, Hawaii, *Geology, 25*, 867-870, doi:10.1130/0091-7613.

Okubo, P. G., J. S. Nakata & R. Y. Koyanagi (2014), The Evolution of Seismic Monitoring Systems at the Hawaiian Volcano Observatory, in Characteristics of Hawaiian Volcanoes, *U.S. Geol. Surv. Professional Paper* 1801, edited by M. P. Poland et al., pp. 67-94.

Park, J., J. K. Morgan, C. A. Zelt, P. G. Okubo, L. Peters & N. Benesh (2007), Comparative velocity structure of active Hawaiian volcanoes from 3-D onshore-offshore seismic tomography, *Earth Planet. Sci. Lett.*, 259, 500– 516, doi:10.1016/j.epsl.2007.05.008.

Park, J., J. K. Morgan, C. A. Zelt & P. G. Okubo (2009), Volcano-tectonic implications of 3-D velocity structures derived from joint active and passive source tomography of the island of Hawaii, *J. Geophys. Res.*, 114, B09301, doi:10.1029/2008JB005929.

Poland, M. P, A. Miklius & E. K. Montgomery-Brown (2014) Magma Supply, Storage, and Transport at Shield-Stage Hawaiian Volcanoes, in Characteristics of Hawaiian Volcanoes, *U.S. Geol. Surv. Professional Paper* 1801, edited by M. P. Poland et al., pp 179-234.

Roux, P. (2009), Passive seismic imaging with directive ambient noise: application to surface waves and the San Andreas Fault in Parkfield, CA, *Geophys. J. Int.*, 179(1), 367-373, doi:10.1111/j.1365-246X.2009.04282.x.

Rowan, L. R. & R. W. Clayton (1993), The three-dimensional structure of Kilauea Volcano, Hawaii, from traveltime tomography, *J. Geophys. Res.*, 98(B3), 4355–4375, doi:10.1029/92JB02531.

Sabra, K. G., P. Gerstoft, P. Roux, W. A. Kuperman & M. C. Fehler (2005a), Extracting time-domain Green's function estimates from ambient seismic noise, *Geophys. Res. Lett.*, 32, L03310, doi:10.1029/2004GL021862.

Sabra, K. G., P. Gerstoft, P. Roux, W. A. Kuperman & M. C. Fehler (2005b), Surface wave tomography from microseism in Southern California, *Geophys. Res. Lett.*, 32, L14311, doi:10.1029/2005GL023155.

Sens-Schönfelder, C. & U. Wegler (2006), Passive image interferometry and seasonal variations of seismic velocities at Merapi Volcano, Indonesia, *Geophys. Res. Lett.*, 33, L21302, doi:10.1029/2006GL027797.

Shapiro, N. M. & M. Campillo (2004), Emergence of broadband Rayleigh waves from correlations of the ambient seismic noise, *Geophys. Res. Lett.*, 31, L07614, doi:10.1029/2004GL019491.

Shapiro, N., M. Campillo, L. Stehly & M. H. Ritzwoller (2005), High-resolution surface-wave tomography from ambient seismic noise, *Science*, 307, 1615-1618, doi:10.1126/science.1108339.

Shapiro, N. M., M. H. Ritzwoller & G. D. Bensen (2006), Source location of the 26 sec microseism from cross-correlations of ambient seismic noise, *Geophys. Res. Lett.*, 33, L18310, doi:10.1029/2006gl027010.

Siebert, L. & T. Simkin (2002-), Volcanoes of the World: an Illustrated Catalog of Holocene Volcanoes and their Eruptions, *Smithsonian Institution*, Global Volcanism Program Digital Information Series, GVP-3, (http://www.volcano.si.edu/world/).

Snieder, R. (2004), Extracting the Green's function from the correlation of coda waves: A derivation based on stationary phase, *Phys. Rev. E*, 69, 046610, doi:10.1103/PhysRevE.69.046610.

Spica, Z., V. M. Cruz-Atienza, G. Reyes-Alfaro, D. Legrand & A. Iglesias (2014), Crustal imaging of western Michoacán and the Jalisco Block, Mexico, from Ambient Seismic Noise, *J. Volcanol. Geotherm. Res.*, 289, 193–201, doi:10.1016/j.jvolgeores.2014.11.005.

Spica, Z., D. Legrand, A. Iglesias, T. R. Walter, S. Heimann, T. Dahm, J.-L. Froger, D. Rémy, S. Bonvalot, M. West & M. Pardo (2015), Hydrothermal and magmatic reservoirs at Lazufre volcanic area, revealed by a high-resolution seismic noise tomography, *Earth Planet. Sci. Lett.*, 421, 27-38, doi:10.1016/j.epsl.2015.03.042.

Stankiewicz, J., T. Ryberg, C. Haberland, Fauzi & D. Natawidjaja (2010), Lake Toba Volcano magma chamber imaged from ambient seismic noise tomography, *Geophys. Res. Lett.*, 37, L17306, doi:10.1029/2010GL044211.

Syracuse, E. M., C. H. Thurber, C. J. Wolfe, P. G. Okubo, J. H. Foster & B. A. Brooks (2010), High-resolution locations of triggered earthquakes and tomographic imaging of Kilauea Volcano's south flank, *J. Geophys. Res.*, 115, B10310, doi:10.1029/2010JB007554.

Tamura, J. & T. Okada (2016), Ambient noise tomography in the Naruko/Onikobe volcanic area, NE Japan: implications for geofluids and seismic activity, *Earth, Planets and Space*, 68:5, doi:10.1186/s40623-016-0380-x.

Thurber, C. H. (1984), Seismic detection of the summit magma complex of Kilauea volcano, Hawaii, *Science*, 223, 165 – 167, doi:10.1126/science.223.4632.165.

Tian, Y. & M. H. Ritzwoller (2015), Directionality of ambient noise on the Juan de Fuca plate: implications for source locations of the primary and secondary microseisms, *Geophys. J. Int.*, 201, 429–443, doi:10.1093/gji/ggv024.

Toomey, D. & G. Foulger (1989), Tomographic inversion of local earthquake data from the Hengill-Grensdalur central volcano complex, Iceland, *J. Geophys. Res.*, 94, 17497-17510.

Tsai V. C. (2009), On establishing the accuracy of noise tomography travel-time measurements in a realistic medium, *Geophys, J. Int.*, 178, 1555-1564, doi:10.1111/j.1365-246X.2009.04239.x.

Weaver, R., B. Froment & M. Campillo (2009), On the correlation of non-isotropically distributed ballistic scalar diffuse waves, *J. Acoust. Soc. Am.*, 126(4), 1817-1826, doi:10.1121/1.3203359.

Webb, S. C. (1998), Broadband seismology and noise under the ocean, *Rev. Geophys.*, 36(1), 105-142, doi:10.1029/97RG02287.

Willis, M., M. Garcés, C. Hetzer & S. Businger (2004), Infrasonic observations of open ocean swells in the Pacific: Deciphering the song of the sea, *Geophys. Res. Lett.*, 31, L19303, doi:10.1029/2004GL020684.

Yang, Y. & D. W. Forsyth (2006), Regional tomographic inversion of the amplitude and phase of Rayleigh waves with 2-D sensitivity kernels, *Geophys. J. Int.*, 166, 1148–1160, doi:10.1111/j.1365-246X.2006.02972.x.

Yang, Y., M. H. Ritzwoller, A. L. Levshin & N. M. Shapiro (2007), Ambient noise Rayleigh wave tomography across Europe, *Geophys. J. Int.*, 168, 259–274 doi:10.1111/j.1365-246X.2006.03203.x.

Yang, Y. J. & M. H. Ritzwoller (2008), Characteristics of ambient seismic noise as a source for surface wave tomography, *Geochem. Geophys. Geosyst.*, 9(2), Q02008, doi:10.1029/2007GC001814.

Yanovskaya, T. B. & T. Y. Koroleva (2011), Effect of earthquakes on ambient noise cross-correlation function, *Izv. Phys. Solid Earth*, 47(9), 747-756, doi:10.1134/S10693513110900059.

Yao, H. J. & R. D. van der Hilst (2009), Analysis of ambient noise energy distribution and phase velocity bias in ambient noise tomography, with application to SE Tibet, *Geophys. J. Int.*, 179(2), 1113-1132, doi:10.1111/j.1365-246X.2009.04329.x.

Zurek, J., G. Williams-Jones, F. Trusdell & S. Martin (2015), The origin of Mauna Loa’s Nīnole Hills: Evidence of rift zone reorganization, *Geophys. Res. Lett.*, 42, 8358–8366, doi:10.1002/2015GL065863.